Physics of Fluids

Characterization of vortical structures in a stirred tank

Cite as: Phys. Fluids **34**, 025127 (2022); https://doi.org/10.1063/5.0083843
Submitted: 30 December 2021 • Accepted: 02 February 2022 • Published Online: 23 February 2022

A. A. Arosemena, H. Ali and J. Solsvik

Physics of Fluids ARTICLE scitation.org/journal/phf

Characterization of vortical structures in a stirred tank

Cite as: Phys. Fluids **34**, 025127 (2022); doi: 10.1063/5.0083843
Submitted: 30 December 2021 · Accepted: 2 February 2022 ·
Published Online: 23 February 2022

View Online Export Citation CrossMark

A. A. Arosemena, H. Ali, and J. Solsvik[a)]

AFFILIATIONS

Department of Chemical Engineering, Norwegian University of Science and Technology (NTNU), NO-7491 Trondheim, Norway

[a)]Author to whom correspondence should be addressed: jannike.solsvik@ntnu.no

ABSTRACT

Data obtained from large eddy simulations of single-phase, turbulent flow of Newtonian and shear-thinning fluids in a baffled stirred tank reactor are considered to identify and characterize vortical structures. The identification proceeds through an objectivized Eulerian method, accounting for the inhomogeneities in the flow, which palliates some shortcomings of previous implementations. The characterization focuses on turbulent vortices larger than the dissipative scales and, to a lesser extent, on trailing and macro-instability vortices. The characterization performed through different statistical analyses includes aspects such as size, number density, shape, distribution and organization in space, and correlation with the kinetic energy due to turbulence and the periodic passage of the blades. To the authors' knowledge, some of these representative aspects have been rarely investigated or have not been addressed at all for the turbulent flow in a stirred vessel. The influence of changing the rotational speed of the tank and the rheology of the working fluid are explored as well. Finally, considering one-way coupling, some potential and practical implications for liquid–liquid and gas–liquid dispersed systems are briefly discussed.

I. INTRODUCTION

Mechanically agitated tanks are widely used in numerous industries for chemical and biochemical processes. A stirred tank has three essential components: (i) a cylindrical vessel containing the working fluid, (ii) a propeller (typically a shafted six-bladed disk/Rushton turbine) generating the swirling motion, and (iii) baffles (commonly four in an equally-spaced configuration) fitted to the walls of the vessel to prevent gross vortexing.[1] A sketch of the typical flow pattern produced in a baffled vessel by a flat-bladed turbine is shown in Fig. 1. The Rushton turbine generates a strong radial discharge, pushing the fluid until reaching the tank walls and thereby creating circulation zones on top and bottom of the propeller region. In stirred tanks, depending upon aspects such as the desired products, the operation may take place under turbulent or locally transitional regimes. Furthermore, the working fluids may be Newtonian but more often than not present more complex rheology. See, e.g., Nouri and Whitelaw,[2] Soos *et al.*,[3] Fernandes del Pozo *et al.*,[4] and Hara *et al.*[5]

Over the last decades, stirred tank reactors have received significant attention and substantial effort has been made to improve our understanding of flow phenomena in these vessels. Broadly speaking, stirred tank studies can be grouped into two categories: experimental investigations and numerical simulations. Experimentally, different visualization techniques, such as particle image velocimetry (PIV), hot-wire anemometry, and laser Doppler velocimetry (LDV), are largely used to investigate flow patterns and acquire instantaneous velocity measurements in stirred vessels (see e.g., Schäfer *et al.*,[6] Sharp and Adrian,[7] Venneker *et al.*,[8] and de Lamotte *et al.*;[9] also, see Mavros[10] for a concise review of different employed experimental techniques). On the other hand, nearly all well-known numerical approaches for turbulent flows in computational fluid dynamics (CFD) have been considered for stirred tank modeling. These include attempted direct numerical simulations (DNS; see Sbrizzai *et al.*,[11] Derksen and den Akker,[12] and Tamburini *et al.*[13]), scale resolving simulations (SRS; see Eggels,[14] Derksen and Van den Akker,[15] Hartmann *et al.*,[16] and Sungkorn *et al.*[17]), and Reynolds-averaged Navier–Stokes simulations (RANS; see Hartmann *et al.*,[16] Singh *et al.*,[18] and Tamburini *et al.*,[19] among many others).

Previous studies (either experimental or numerical), for the most part, have focused on flow patterns, turbulence intensities, turbulent kinetic energy, and dissipation rates. Changes due to different types of impellers, vessel configurations, Reynolds numbers, and working fluid rheology have been explored as well. These properties, geometrical features, and operational aspects are of interest due to their relevance in mixing and transport phenomena within the agitated tank. For instance, flow patterns are known to influence mixing performance at the largest scales (macromixing), while the turbulent dissipation rate is

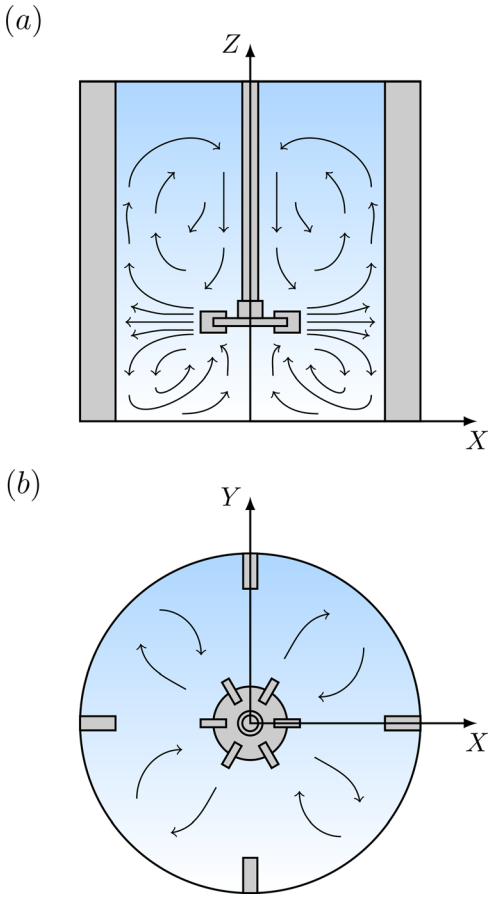

FIG. 1. Illustration of the flow pattern produced by a Rushton-type impeller in a baffled tank: (a) cross-sectional view and (b) top view.

important for both dispersion of fluid particles (drops and bubbles) and mass transfer in multiphase systems; see Garcia–Ochoa and Gomez[20] for a review about gas–liquid mass transfer in a bioprocess where the dissipation rate is identified as one of the main factors affecting the oxygen transfer rate. In addition, topics such as turbulence anisotropy for modeling of realizable states of turbulence,[21] local shear-rate quantification,[22] and identification of coherent vortical structures (starting with the tomographic observations of Takashima and Mochizuki[23]) have also been addressed in studies about stirred tanks, albeit perhaps to a lesser extent.

Vortices are swirling-like structures, which play a major role in turbulence. The popular quote by Richardson,[24] broadly describing the direct energy cascade process, constitutes a memorable illustration of such a role. In a mechanically agitated vessel, these structures are clearly important not only for the cascade process but also for actual mixing (at the molecular level) and particle dispersion and coalescence; many models for fluid particle breakup and coalescence in dispersed turbulent flow systems are based on particle–eddy interaction mechanisms (see Liao and Lucas[25,26] and Solsvik *et al.*[27] for reviews of these models). As illustration, in the context of deformation and breakup of fluid particles, consider Kresta and Brodkey[28] who presented different particle responses depending on the size and intensity of the surrounding eddies. A droplet may be simply advected when interacting with a much larger eddy, whereas it may deform or even breakup in daughter particles when the interacting eddies are of comparable size or much smaller than the size of the original droplet. It is worth mentioning that despite vortices of different sizes being encountered in stirred tanks, trailing/tip vortices at an intermediate scale and those related to flow macroinstabilities (MIs) are the most studied.

Trailing vortices are counter-rotating vortex pairs generated behind the upper and lower edges of each impeller blade due to their periodic passage.[29–31] Trailing vortices have been subject of extensive research because of the seemly strong correlation between them and regions of high vorticity, strain rate, turbulent dissipation, and Reynolds stresses; see e.g., Yianneskis *et al.*,[32] Stoots and Calabrese,[33] Lee and Yianneskis,[34] Derksen *et al.*,[35] Sharp and Adrian,[7] Escudié and Liné,[36] Escudié *et al.*,[37] Bouremel *et al.*,[38] Sharp *et al.*,[39] Chara *et al.*,[40] among others. Aside reporting turbulent quantities in the near-impeller region, some of these authors have also attempted to characterize the trailing vortices by identifying their cores and corresponding mean trajectories, surface area (indicative of vortex size), and velocity circulation (indicative of vortex strength). Meanwhile, MIs are temporal mean flow variations affecting the flow patterns and stemming from changes of impeller off-bottom clearance, changes in Reynolds numbers, and/or precessional motion of a vortex (or vortices) around the impeller shaft.[41,42] MIs vortices were first identified by Yianneskis *et al.*[32] as low-frequency, "whirlpool"-like type of vortex precessing around the shaft in which characterization started with their frequency at different impeller designs, impeller clearances,[41] and Reynolds numbers.[42] Further information, such as the trajectory of these structures[43] and their interaction with trailing vortices,[44] has also been reported for mixing enhancement purposes.

The present work aims to identify and characterize vortical structures. The input flow fields are obtained from large eddy simulations of single-phase, turbulent flow of Generalized Newtonian (GN) fluids[45] in a baffled stirred tank reactor. Different from previous investigations, the identification is performed using a fully frame invariant version of an Eulerian local region-type method, which takes into account that the stirred flow is inhomogeneous in all spatial directions. The characterization includes representative aspects of the identified structures that have been rarely investigated or have not been addressed at all in the context of stirred tanks and focuses on turbulent vortices larger than the dissipative scales and, to a lesser extent, on trailing and MI vortices. The effects of having different rotational speeds and shear-thinning rheology (in comparison with Newtonian fluids) are also explored. Some potential and practical implications for liquid–liquid and gas–liquid dispersed systems, where the local fraction of the dispersed phase (holdup) is always sufficiently small, are briefly discussed as well.

This paper is organized as follows. The used numerical approach, the considered fluid flow cases, and other computational details, such as impeller motion treatment or employed grid, are described in Sec. II. Eulerian methods that are commonly used for the identification of vortical structures and their main weaknesses when considering flows due to induced swirling motion are outlined in Sec. III. Section III also describes the considered vortex identification method, which is not only Galilean invariant but also observer-independent, and different regions of potential interest in the stirred vessel. The characterization of the identified structures, including aspects such as size, number

TABLE I. Physical properties, Carreau model parameters, and Reynolds number of the fluid flow cases under study. Here, W600 and C600 denote the cases where the stirred vessel is operated at 600 rpm, whereas W800 and C800 denote the cases where it is operated at 800 rpm. *Re* is the Reynolds number based on the impeller rotational speed $N(\text{rev s}^{-1})$, its diameter D; see Subsection II D, and μ_a for an average strain rate according to the Metzner–Otto correlation for a Rushton-type stirrer;[50] i.e., $k_s N \approx 11.5N$. k_s is the Metzner constant.

Case	Fluid	Line/marker color	$\rho \times 10^3$ (kg m^{-3})	$\mu_0 \times 10^{-3}$ (Pa s)	$\mu_\infty \times 10^{-3}$ (Pa s)	λ (s)	α $(\cdots)$	$Re = \rho N D^2/\mu_a$ $(\cdots)$
W600	Water	Black	1.00	1.00	⋯	⋯	1.000 0	49 000
W800	Water	Black	1.00	1.00	⋯	⋯	1.000 0	65 333
C600	CMC 0.2%	Red	1.00	97.40	14.80	0.281 5	0.689 2	1144
C800	CMC 0.2%	Red	1.00	97.40	14.80	0.281 5	0.689 2	1616

density, shape, distribution and organization in space, and the correlation between the vortex indicator and the kinetic energy due to turbulence and the periodic passage of the blades, is addressed in Sec. IV. Finally, a summary of our main findings, some possible implications in terms of multiphase systems, and further work are presented in Sec. V.

II. NUMERICAL PROCEDURE

A. Large-eddy simulations (LES)

In the LES approach, large grid scales are resolved while the smallest, subgrid-scales (SGS) are modeled. The smallest scales are supposed to be more isotropic and more in equilibrium than the large scales. Moreover, the smallest scales only contain a minor fraction of the total turbulent kinetic energy. The governing equations in LES are obtained by spatially filtering the governing equations for mass and momentum conservation. For incompressible GN fluids, in the absence of external forces, the filtered equations read as

$$\frac{\partial \widetilde{u}_i}{\partial x_i} = 0, \tag{1}$$

$$\frac{\partial \widetilde{u}_i}{\partial t} + \frac{\partial(\widetilde{u}_i \widetilde{u}_j)}{\partial x_j} = -\frac{1}{\rho}\frac{\partial \widetilde{p}}{\partial x_i} + \frac{1}{\rho}\frac{\partial}{\partial x_j}\left(2\widetilde{\mu_a \mathrm{S}_{ij}}\right) - \frac{\partial \tau_{ij}}{\partial x_j}, \tag{2}$$

where $\widetilde{(\,)}$ indicates a grid-filtered variable, x_i and u_i denote the spatial-Cartesian coordinates and the instantaneous velocity field, respectively, and t represents time while ρ is the fluid density and p is the pressure field. In Eq. (2), μ_a is the apparent dynamic viscosity, which, for a GN fluid, solely depends on the strain rate $\dot{\gamma} = (2\mathrm{S}_{ij}\mathrm{S}_{ij})^{1/2}$, and $\mathrm{S}_{ij} = (\partial u_i/\partial x_j + \partial u_j/\partial x_i)/2$ is the strain rate tensor. In this paper, when index notation is used, subscript i (or any other subscript) takes the value 1, 2, or 3 to represent the X, Y, or Z component, respectively. In the stirred vessel, the Cartesian coordinate system is as shown in Fig. 1.

The SGS- or residual stress tensor τ_{ij}, introduced after filtering the momentum equation, is defined as

$$\tau_{ij} = \widetilde{u_i u_j} - \widetilde{u}_i \widetilde{u}_j, \tag{3}$$

which is to be modeled. The SGS-stress tensor for a shear-dependent GN fluid is treated in the same manner as for a Newtonian fluid[17] and modeled through the Smagorinsky–Lilly model[46,47] as

$$\tau_{ij} - \frac{1}{3}\delta_{ij}\tau_{kk} = -2\nu_{sgs}\widetilde{\mathrm{S}}_{ij} = -2\left[\ell_{sgs}^2\left(2\widetilde{\mathrm{S}}_{ij}\widetilde{\mathrm{S}}_{ij}\right)^{1/2}\right]\widetilde{\mathrm{S}}_{ij}. \tag{4}$$

In SGS-kinematic viscosity ν_{sgs}, SGS-length ℓ_{sgs} is given by

$$\ell_{sgs} = \min(C_s\Delta, \kappa d). \tag{5}$$

Here, C_s is the flow-dependent Smagorinsky "constant," Δ is the local grid size based on the volume of the corresponding computational cell, $\kappa \approx 0.4$ is the von Kármán constant, and d is the distance to the nearest wall. For stirred tank flow, the optimal value for C_s has yet to be determined.[12] In this work, as in Fan *et al.*[48] and Devi and Kumar,[49] C_s is set as 0.1.

B. Fluid rheology

In simulations, shear-dependent rheology is incorporated through the Carreau fluid model (see, e.g., Irgens[45]) i.e.,

$$\mu_a = \mu_\infty + (\mu_0 - \mu_\infty)\left[1 + (\lambda\dot{\gamma})^2\right]^{(\alpha-1)/2}, \tag{6}$$

where μ_∞ and μ_0 are the "infinite" and "zero" shear rate viscosities, respectively, λ is a time constant, and α is the flow index, which, for shear-thinning, is to be less than unity. Newtonian fluid behavior is recovered for $\alpha = 1$. The values for different physical properties and Carreau model parameters of the fluids under study, water and 0.2 wt. % carboxymethyl cellulose (CMC) solution, are presented in Table I. The corresponding viscosity rheogram for the shear-thinning fluid case (CMC 0.2%) is shown in Fig. 2.

C. Impeller motion treatment

The rotational motion of the impeller adds complexity to the simulations. For baffled stirred tanks, the contradiction between the rotating impeller and the stationary baffles requires specific numerical treatment.[51] Modeling is typically performed using either the multiple

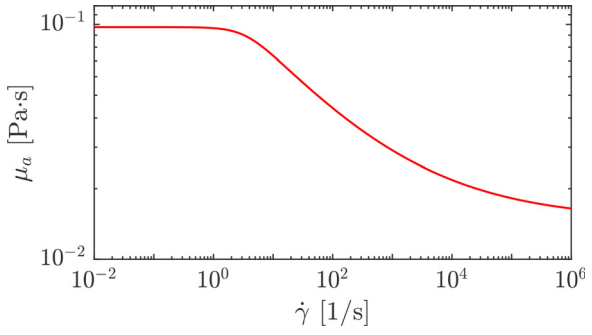

FIG. 2. Apparent viscosity as a function of the strain rate, μ_a vs $\dot{\gamma}$, for 0.2 wt. % CMC solution.

reference frame (MRF, Luo *et al.*[52]) or the sliding mesh (SM, Murthy *et al.*[53]) approach. The MRF approach is a steady-state approximation for stirred tanks having a weak impeller-baffle interaction. In the MRF method, the computational mesh is fixed at the beginning of simulation and the domain is divided into an impeller zone (using a rotating reference frame) and a stationary zone (using a stationary reference frame). On the other hand, the SM technique is a fully transient approach where the rotational motion of the impeller is explicitly taken into account.[54] In the SM approach, the computational domain is also divided into two non-overlapping submeshes, one rotating with the impeller while the other is fixed as in the MRF method. However, the SM method allows the adjacent meshes to slide relative to one another and the coupling along the sliding interface is accounted for by re-establishing the cell connectivity each time when sliding occurs.[51] In other words, as the computation proceeds and the impeller moves in a periodic manner, the computational mesh is adjusted accordingly. The SM approach is considered as a more accurate method for unsteady state simulations in stirred tanks, and it is used in this work.

D. Computational aspects

Simulations were performed for a laboratory-scale, 11 L stirred tank. Table I summarizes the considered flow cases, and Fig. 3 shows the stirred vessel configuration. The corresponding geometrical details are as follows: tank diameter $T = 24$ cm, fluid column height $H = T$, baffles width $w_{bf} = T/9.6$, baffles thickness $t_{bf} = T/24$, off-bottom clearance $C = 7$ cm, impeller diameter $D = C$, impeller diameter without blades $D_i = 5.2$ cm, blades height $h_b = 1.5$ cm, blades width $w_b = 1.8$ cm, blades thickness $t_b = 0.2$ cm, outer diameter of shaft $DS_o = 1.2$ cm, and inner diameter of shaft $DS_i = 1$ cm.

The computational domain was enclosed between two main parts: an inner rotating cylinder, consisting of the shaft and impeller, and an outer stationary cylinder containing the baffles and rest of the tank. The domain was discretized with structured hexahedral elements using Ansys ICEM (version 19.1, Ansys, Inc., Canonsburg, PA). The inner rotating cylinder region and regions near wall boundaries and edges were discretized using finer cells than those used in other regions of the tank. Boundary layers were specified to resolve the flow effects near to the walls of the stirred tank. The boundary layers were defined using a first layer thickness approach. The total number of boundary layers was five, and the first layer thickness was set to 0.2 mm. This is the minimum grid size while the maximum size goes up to 4 mm. The grid quality was checked by computing the determinant of hexahedral elements. The determinant test computes the deformation of the elements by calculating the Jacobian of each hexahedron and then normalizing the determinant of the matrix. Determinant values above 0.3 are acceptable for most commercial solvers and, in this work, the minimum and maximum values of the determinant were 0.764 and 1, respectively. It is worth commenting that the mesh size was selected after performing a grid sensitivity analysis. In the tests, the grid size of the stirred tank was scaled by a factor of 2 (see Table II). For different axial positions and for a radial coordinate close to the edge of the impeller blades, the radial, axial, and tangential velocity components for water and CMC 0.2% cases were computed and compared for all grid sizes as shown in Table II. A slight difference (1%–3%) between the computed values of the velocity components using grid sizes G2 and G3 was found, and thus, G2 was selected for conducting all the simulations. Table II also shows the near-wall resolution, y^+, for different grids and when water is the working fluid. To the best of the authors' knowledge, in most rotation flow problems, the grid is generally considered well resolved with $y^+ < 40$. See Fig. 4 for an illustration of the employed grid distribution, G2. With respect to the boundary conditions, the inner rotating cylinder containing the impeller and shaft was specified with rotational speed (rpm). The contact boundary between the inner rotating cylinder and outer stationary cylinder was set as interface. The top surface of the tank was set to no-slip boundary condition to mimic the placement of a lid at the top

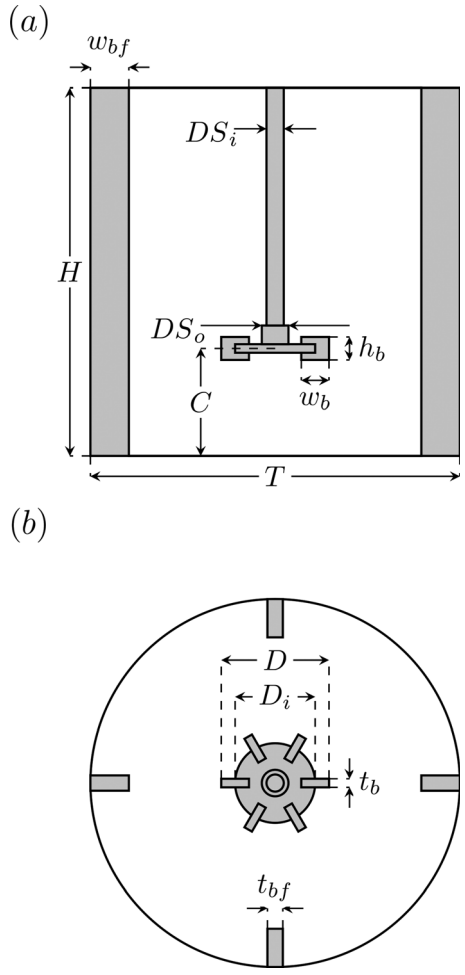

FIG. 3. Stirred tank configuration: (a) cross-sectional view and (b) top view.

TABLE II. Grids considered during sensitivity analysis.

Grid label	Number of cells (10^6)	Number of nodes (10^6)	y^+
G1	0.845	0.891	23.8
G2	1.570	1.631	19.5
G3	3.146	3.249	12.5

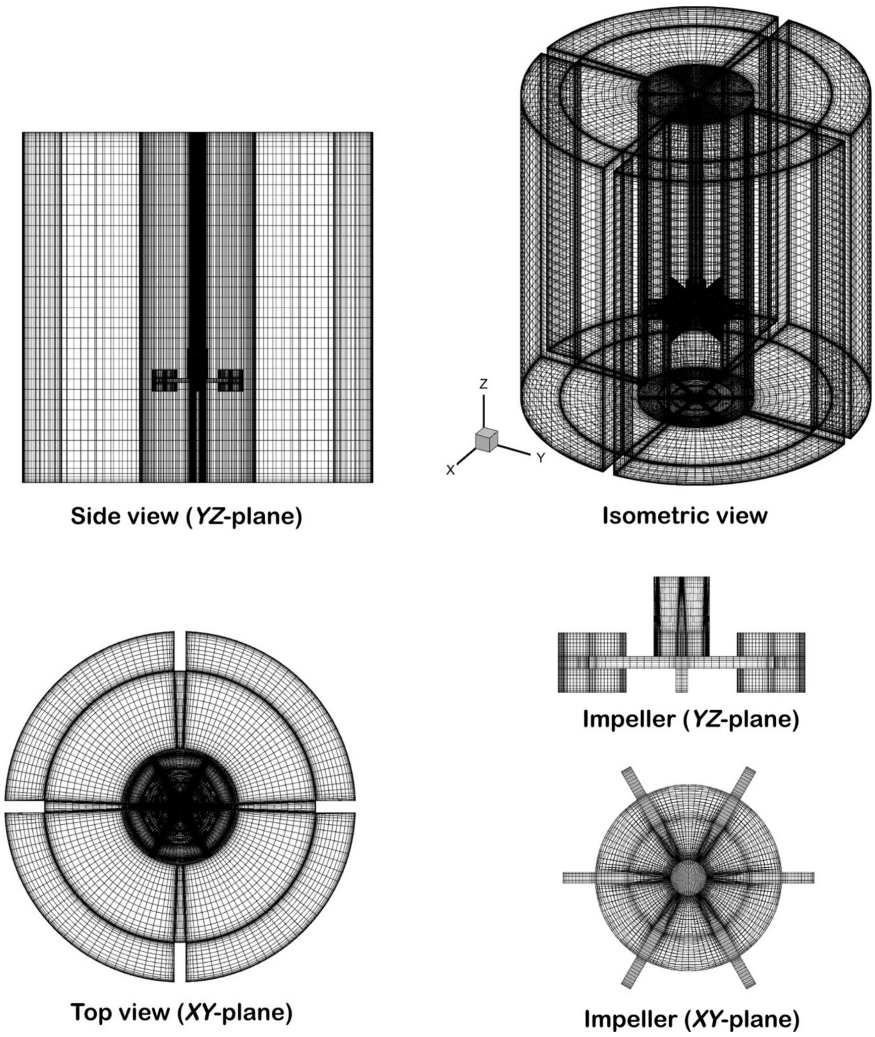

FIG. 4. Illustration of the computational mesh used for large eddy simulations of the baffled stirred tank.

surface in experiments to avoid the formation of air bubbles in the liquid. All other remaining boundaries were specified with no-slip and impermeability boundary conditions.

LES were performed using a finite volume based-method through the commercial package, Ansys FLUENT (version 19.1, Ansys, Inc., Canonsburg, PA). In this software, the term in parentheses, appearing on the right-hand side of Eq. (2), is approximated as $\mu_a \widetilde{S}_{ij}$. Also, μ_a is calculated considering a strain rate based on the resolved flow field. The discretized governing equations were solved using the algebraic multigrid method. The bounded central differencing scheme was used for the spatial discretization of the cell-face values of the transported field in the momentum equation. Meanwhile, Green–Gauss node-based and second-order schemes were used for the evaluation of gradients and for interpolating the pressure values at the cell–faces, respectively. A second order implicit scheme was used for the temporal formulation. Coupling between the continuity and momentum equations was done using the pressure-based SIMPLEC segregated algorithm.

Computations were initialized with the results obtained from steady RANS (realizable version of $k-\varepsilon$ eddy-viscosity model; Launder and Spalding[55]) simulations. These simulations were conducted with a time step of 0.2 ms (corresponding to 1° of impeller rotation). The number of iterations per time step was set to 50 for ensuring that every residual parameter reached the set absolute convergence criteria of 1×10^{-5}. A total number of 27 000 time steps were performed, corresponding to at least 35 impeller revolutions. The volume-averaged torque and turbulent kinetic energy were monitored during LES and after 10–13 impeller revolutions, the system reached quasi-steady state. Afterward, for each fluid flow case, instantaneous realizations of the grid-resolved velocity field in the Cartesian coordinate system, i.e., $\widetilde{u}_i = \widetilde{u}_i(x_i, t)$, were exported and a total of 1700 flow fields were collected for post-processing into our own in-house FORTRAN scripts. For simplicity, hereafter the tilde is dropped and, unless otherwise stated, a variable without tilde should be interpreted as a grid-resolved one, $u_i \equiv \widetilde{u}_i$. All simulations were performed on Fram, a Norwegian national high-performance computing (HPC) system, and each simulation case consumed about 50 000 CPU hours. Post-processing consisting of the identification of vortical structures

and computation of other relevant statistics was carried out on the Idun cluster, a local NTNU HPC-facility.

III. VORTEX IDENTIFICATION METHOD

As remarked in the Introduction, the identification and consequent understanding of vortices is of paramount importance for mixing in stirred tanks. Our intuition associates vortical structures with circular patterns seen in a flow; however, until today, there is no formal (mathematical) definition of a "vortex," which is unanimously recognized by the fluid dynamics community. For instance, when looking at a vortex as a finite structure, it is difficult to agree on its extension, i.e., where the vortex ends.[56] This lack of an accepted definition hinders their identification and explains the emergence of multiple criteria for vortex detection during the last decades. Vortex identification methods can be broadly classified as Lagrangian and Eulerian (see Epps[57] for a recent comprehensive review). The most popular vortex identification methods such as the Q-criterion,[58] the Δ-criterion[59] or the λ_2-criterion[60] are region-type methods, where vortex cores are defined within regions where a scalar field based on e.g., local or point-wise values of the velocity gradient tensor, $D_{ij} = \partial u_i/\partial x_j$, exceeds or not a certain threshold.

The aforementioned Eulerian local region-type methods are conceptually easy to explain in the sense that a vortex exists if the considered criterion is met and typically have clear physical meaning such as a vortex represents regions of coherent swirling motion (swirling-strength criterion, Zhou *et al.*[61]) or a vortex is a local region where there is an excess of rotation rate relative to strain rate (Q-criterion; see Chakraborty *et al.*[62]). Moreover, since these methods can be computed in a point-wise manner and only depend on the instantaneous velocity field, their computation can be parallelized and they adapt instantaneously to an evolving unsteady flow field.[57] Nevertheless, these identification methods have also several shortcomings (see, e.g., Kolář[63]) such as their inability to provide the same results in different rotation frames (i.e., material objectivity or frame invariance, see Haller[64]) or their sensitivity to the selected threshold value; that is, different vortical structures are visualized at different thresholds (see, e.g., Liu *et al.*[65]).

For industrial equipment where swirling motion is induced by rotating mechanical parts, such as turbomachines or stirred-tank reactors, material objectivity is particularly desirable; unless rotational invariance is fulfilled, different observers applying these methods (e.g., Q and Δ criteria) in their own frame of reference will identify different regions as vortical structures.[66] In this regard, recently, Haller[67] remarked that in the available objectivization procedures for these local vortex criteria, only the replacement of the spin/rotation rate tensor by a spin-deviation tensor defines compatible local observers for arbitrary fluid flows. Here, the idea is to compute the spin-deviation tensor as the difference between the original rotation rate tensor and its instantaneous spatially averaged value obtained from the instantaneous spatially averaged vorticity field; see Haller *et al.*[68] The procedure was proposed and implemented by Liu *et al.*[69] and Liu *et al.*[70] to objectivize the Rortex criterion[71–73] and the omega method.[65]

The other issue, about the threshold sensitivity of these Eulerian methods, comprises (i) the (potential) spatial dependency of the threshold in the case of inhomogeneous flows and, perhaps more importantly, (ii) the absence of a general procedure that removes the user-subjective approach in the selection of threshold values. The first aspect can be addressed considering a non-uniform threshold based on a statistical indicator of the criterion used for the vortex detection. Nagaosa and Handler[74] proposed a threshold varying in the wall-direction with the standard deviation of the Q-values for (canonical) turbulent channel flow. Thereupon, the idea of using the standard deviation of the considered Eulerian criterion to take into account inhomogeneities in the flow has been successfully employed by multiple authors (see, e.g., del Álamo *et al.*,[75] Lozano-Durán *et al.*,[76] and Cheng *et al.*[77]). The second aspect, about the arbitrary selection of thresholds, can be palliated considering the percolation crisis analysis introduced by Moisy and Jiménez[78] (see, e.g., del Álamo *et al.*,[75] Lozano-Durán *et al.*,[76] Dong *et al.*,[79] Hwang and Sung,[80] Osawa and Jiménez,[81] and Cheng *et al.*[77]). In this procedure, different thresholds are evaluated to examine where a perceptible transition from a highly clustered region to increasing individual structures identified according to a particular method (e.g., Q or Δ-criterion) occurs. The threshold at which the percolation transition/crisis takes place is considered a critical one, and the threshold for proper visualization of the structures lies above it. Nonetheless, it is still up to the researcher to decide how large the selected threshold should be with respect to the critical one. For this reason, the clustering methodology is often accompanied by a sensitivity analysis where the influence of the selected threshold is briefly studied.

In the case of stirred-tank devices, previous studies have mostly implemented nonobjective and threshold sensitive vortex identification methods. Escudié *et al.*[37] used the λ_2-criterion to identify vortex cores of trailing vortices, and Escudié *et al.*[37] and Escudié and Liné[82] remarked that earlier investigations localize trailing vortices either (i) from the phase-averaged velocity fields, where for a given angular position of the measurement plane compared to the blade, the vortex center is defined by the location where the vertical velocity is zero or (ii) from a dimensionless vorticity calculated in a vertical plane of measurement relative to the blade position, which had to exceed an arbitrary threshold value for the detection of a vortex core. Afterward, the λ_2-criterion gained significant popularity and has been used for the identification of both trailing and MI-vortices; see e.g., Ducci and Yianneskis,[43] Chara *et al.*,[40] and Başbuğ *et al.*[83] In recent years, aside the λ_2-criterion, other methods such as the swirling-strength criterion (see Sharp *et al.*[39] and Singh *et al.*[18]) or the standard Q-criterion (see Zamiri and Chung[84]) have been implemented as well. Nevertheless, these methods present the same shortcomings. In this work, vortical structures are identified using an Eulerian local region-type method, which should be fully frame invariant, take into account that the flow is inhomogeneous in all spatial directions and also lead to consistent results even if slightly different threshold values are used. Subsection III A describes the procedure employed to identify the vortical structures.

A. An objectivized version of the Q-criterion

The previously mentioned velocity-gradient-based vortex identification criteria (see Sec. III) are Galilean invariant, i.e., invariant under translation of frames but not material objective since the angular rotation rates in the spin tensor are (implicitly) measured relative to the reference frame of the observer.[57] Eulerian methods based on instantaneous point-wise values of D_{ij} can be objectivized by replacing the velocity gradient tensor with a net version of it, defined as[67,69]

$$D_{ij\star} = S_{ij} + \left(\Omega_{ij} - \langle\Omega_{ij}\rangle\right), \tag{7}$$

where $D_{ij\star}$ is a net velocity gradient tensor, $\Omega_{ij} = (\partial u_i/\partial x_j - \partial u_j/\partial x_i)/2$ is the spin/rotation rate tensor, and $\langle\Omega_{ij}\rangle = -\varepsilon_{ijk}\langle\omega_k\rangle/2$ is a spatially averaged spin tensor based on a spatially averaged vorticity, $\langle\omega_k\rangle$. Here, ε_{ijk} is the alternation or Levi–Civita tensor. Haller *et al.*[68] defines this instantaneous spatially averaged vorticity as

$$\langle\omega_k\rangle = \frac{1}{\mathcal{V}}\int_{\mathcal{V}} \omega_k \mathrm{d}\mathcal{V}, \tag{8}$$

where $\mathcal{V}$ is the volume of the flow domain. From Eq. (7), we can easily define objective versions of the different well-known vortex identification criteria.

The objectivized version of the Q-criterion,[58] in the context of incompressible flows, can be expressed as

$$Q_\star = -\frac{1}{2}\left(D_{ij\star}D_{ji\star}\right) = \frac{1}{2}\left(\Omega_{ij\star}\Omega_{ij\star} - S_{ij}S_{ij}\right) > 0, \tag{9}$$

where $Q_\star$ denotes the considered objective version of the Q-criterion and $\Omega_{ij\star} = \Omega_{ij} - \langle\Omega_{ij}\rangle$ is the corresponding net spin tensor. In this work, we have decided to use the $Q_\star$-criterion to identify vortical structures in the stirred tank considering that the classical Q-criterion is one of the most commonly used vortex identification methods (see, e.g., Mihalić *et al.*[85] for an application in turbomachinery or Wang *et al.*[86] for an application in design of marine propellers). Conceptually, $Q_\star > 0$ defines a vortex as a connected fluid region where there is more net rotation than stretching; however, similar to the original criterion, a non-zero threshold value is required for the identification of (distinct) individual structures. Moreover, this threshold should account for the fact that the swirling flow in the stirred tank is inhomogeneous in all spatial directions and its selection should not be arbitrary.

Following the arguments presented above, at a given instant, we consider that a grid point in the spatial domain belongs to a vortex if

$$Q_\star \geq \mathcal{T}\,\mathrm{stv}(Q_\star), \tag{10}$$

where $\mathcal{T}$ is the thresholding parameter and $\mathrm{stv}(Q_\star)$ is the standard deviation of the $Q_\star$-values and the selected statistical indicator to take into account inhomogeneities in the flow. Here, for a given $\mathcal{T}$, neighboring grid points satisfying Eq. (10) are connected, merged, and classified as individual structures. Connectivity is defined by the six orthogonal nearest neighbors of each grid point, and the $\mathcal{T}$-parameter is chosen following a percolation crisis analysis. In a percolation analysis, the ratio between the volume of the largest structure, V_{max}, and the total volume occupied by all the structures, V_{tot}, is computed for different values of $\mathcal{T}$. Here, as mentioned in Sec. III, the idea is to set a threshold larger than that of the critical one for proper visualization. The critical threshold corresponds to the $\mathcal{T}$-value where the percolation transition occurs, i.e., where the change of the ratio with respect to $\mathcal{T}$ attains a minimum. Before the critical threshold, most of the domain is occupied by large objects, and in practice, it is not possible to distinguish individual structures. In percolation analysis, aside the V_{max}/V_{tot}-ratio, the ratio between the total number of identified objects at a given $\mathcal{T}$, N_{tot}, to the largest number of identified structures' overall $\mathcal{T}$-values, N_{max}, is often studied as well.

For a wide range of $\mathcal{T}$-values, Fig. 5(a) displays the time average of the V_{max}/V_{tot}-ratio, whereas Fig. 5(b) shows the time average of the N_{tot}/N_{max}-ratio. Considering these percolation diagrams, we observe the following:

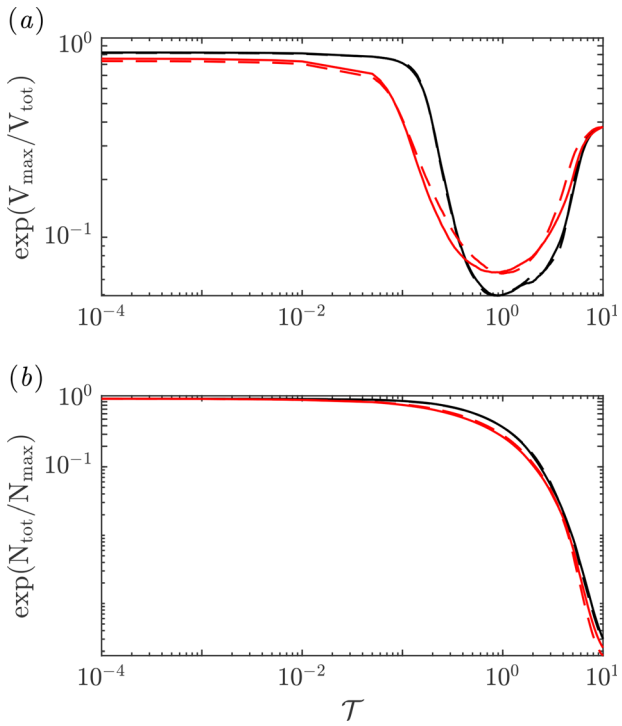

FIG. 5. Percolation diagrams: (a) $\exp(V_{max}/V_{tot})$ and (b) $\exp(N_{tot}/N_{max})$. Here, $\exp(\,)$ denotes an expectation or time-averaged quantity. Cases where the impeller operates at 800 and 600 rpm are identified by the line styles "——" and "- - -," respectively. Colors as explained in Table I.

(i) Before the percolation transition takes place, the largest identified object occupies most of the domain. Moreover, the maximum (possible) number of structures is detected as well.

(ii) The percolation transition starts at the critical threshold and goes up to $\mathcal{T} \approx 1$. For cases C600, C800, W600, and W800, the critical threshold is about 0.073, 0.077, 0.177, and 0.179, respectively.

(iii) The percolation transition appears to delay (slightly) with an increase of Reynolds number, *Re*, but this fact alone is not deemed sufficient to explain the difference between the profiles corresponding to Newtonian and shear-thinning fluid cases for a given impeller rotational speed, *N*. The overall decrease in the number of structures with shear-thinning behavior is probably the main reason for the difference in the percolation transition. A cluster of objects leading to a less populated domain is likely to fall apart more promptly.

In summary, the clustering methodology allows us to recognize the lowest practical threshold for which the vortices can still be identified individually, i.e., the critical one. Here, for comparison purposes and for more easily distinguish the individual structures, $\mathcal{T}$ is set to 1 for all fluid flow cases. At such a threshold, between 30% and 40% of

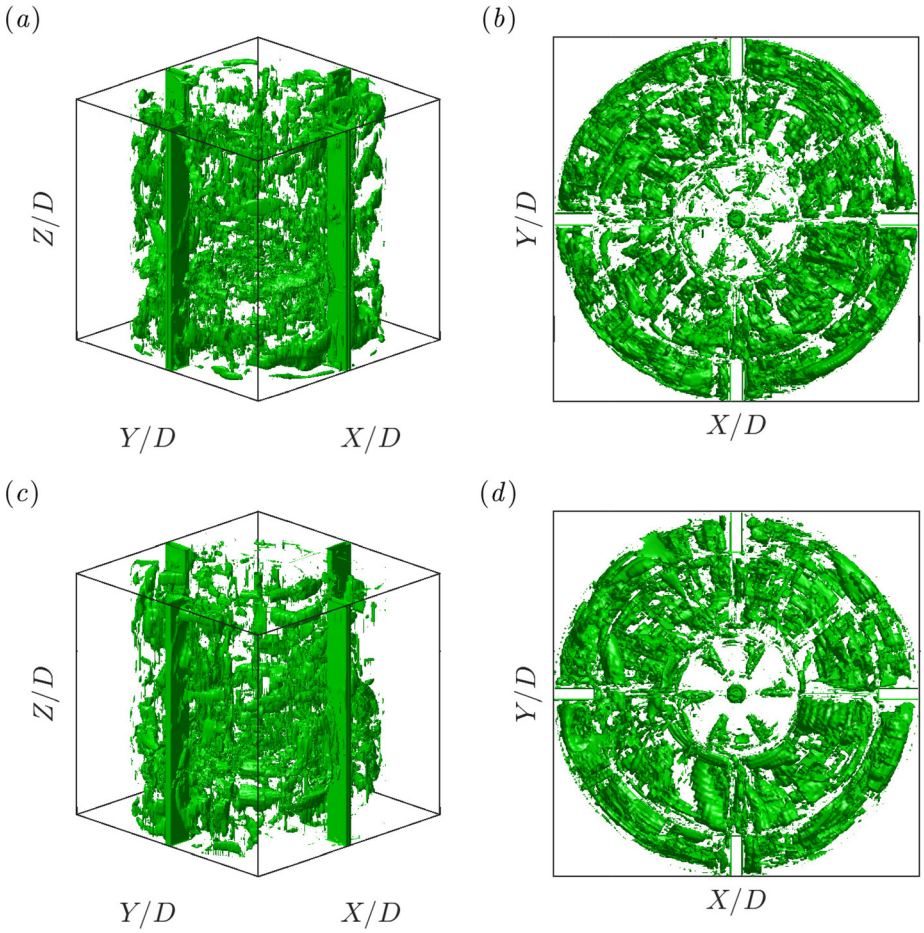

FIG. 6. Instantaneous vortical structures identified by the isosurfaces of $Q_\star/\mathrm{stv}(Q_\star) = 1$ for (a), (b) W800 and (c), (d) C800. 3 D view displayed in (a), (c) and top view in (b), (d). Fluid flow cases as described in Table I.

the maximum (possible) number of structures are identified and the largest object does not occupy most of the domain. Due to the computational cost, a sensitivity analysis of the results to the selected threshold is not performed. Nonetheless, considering previous works (see, e.g., Cheng *et al.*[77] and Arosemena *et al.*[87]) and for threshold values larger than the that of the critical one, it is deemed probable that consistent trends in the results will be observed when the threshold value is changed to another one differing by less than an order-of-magnitude.

Figure 6 shows the vortical structures identified by criterion (10) with $\mathcal{T} = 1$ for the Newtonian and shear-thinning fluid cases when the stirred tank operates at 800 rpm. Here, despite using a threshold value close to the end of the percolation transition, it is still challenging to interpret the results. Nevertheless, from the figure, we note an apparent increase in the size of the objects and an overall decrease in the number of detected structures for the shear-thinning fluid case. Furthermore, for both the cases, some regions in the tank seem more populated than others and the range of scales of the vortices probably varies as well.

B. Regions of potential interest in a stirred tank

Regardless of the fluid flow case, the identified vortical structures in the stirred tank appear to be complex, being highly three-dimensional and presenting a wide range of scales. Considering Fig. 6, as we move in a circular manner from the tank's center toward its wall, the following three distinct regions are seen:

(i) $r = \sqrt{X^2 + Y^2} \in [0, 0.5D]$, i.e., up to the impeller. This region in comparison with the others does not seem as highly populated. Moreover, the size of the structures appears more moderated and the range of scales narrower.

(ii) $r \in (0.5D, 0.396T]$, i.e., approximately up to the baffles. Here, a larger range of scales is seen and, compared to (i), this region is more populated.

(iii) $r \in (0.396T, 0.5T]$, i.e., up to the tank's wall. In this region, compared to (i) and (ii), sizable structures are mostly seen. Visually, this also make it difficult to determine if region (iii) is more populated than (i) and (ii).

Likewise, distinct features are expected in the axial direction, as we move from bottom of the tank up to its top. However, based on Fig. 6, it is not evident which regions are the most populated or which ones present a wider range of spatial scales. Having said that, it is also well-known that the trailing vortices are generated behind the upper and lower edges of each blade, which makes the impeller region and those right next to it, compelling targets for investigation.

TABLE III. Subdomains of potential interest in a stirred tank.

Label	Regions covered	Resulting volume
SUB-A	(i)-(a)	$\pi(0.5D)^2(C-0.5h_b)$
SUB-B	(i)-(b)	$[\pi((0.5D)^2-(0.5D_i)^2)-6t_b(0.5w_b)]h_b$
SUB-C	(i)-(c)	$\pi[(0.5D)^2-(0.5DS_i)^2](T-C-0.5h_b)$
SUB-D	(ii)-(a)	$\pi[(0.396T)^2-(0.5D)^2](C-0.5h_b)$
SUB-E	(ii)-(b)	$\pi[(0.396T)^2-(0.5D)^2]h_b$
SUB-F	(ii)-(c)	$\pi[(0.396T)^2-(0.5D)^2](T-C-0.5h_b)$

In consequence, there are (at least) three regions of potential interest in the axial direction:

(a) $Z \in [0, C-0.5h_b]$, i.e., up to the lower edge of each impeller blade. This is the lower circulation loop region (see illustration in Fig. 1).
(b) $Z \in (C-0.5h_b, C+0.5h_b]$, i.e., up to the upper edge of each impeller blade. This is the impeller region.
(c) $Z \in (C+0.5h_b, T]$ constituting the remaining part of the tank where the upper circulation loop is observed (see illustration in Fig. 1). It is worth remarking that the upper circulation loop does not extend to the top of the tank and there is a badly mixed region occupying 14%–18% of the total tank volume.[16] In the case of shear-thinning fluid rheology, such a badly mixed region is probably larger.

The regions of potential interest in the stirred tank lead to certain subdomains and, most of them, are summarized in Table III. Here, six different subdomains consisting of either cylindrical or tube-like volumes are considered (see Fig. 7). It is noted that the seemingly clustered region of structures between baffles and tank wall is not explored. The characterization of the identified vortices in these subdomains of potential interest is presented in Sec. IV. Here, a vortical structure is included in the analysis of a particular subdomain if the centroid of such a structure, (X_c, Y_c, Z_c), is encountered in that subdomain. Further details about spatial distribution of the detected vortices are discussed in Subsection IV C.

IV. CHARACTERIZATION OF VORTICAL STRUCTURES

Before continuing with Subsections IV A–IV D, we would like to stress that although the presented results correspond to single-phase flow simulations, their discussion is vastly motivated by the possible implications in multiphase flow systems. This is particularly the case for systems in which the local fraction of the dispersed phase is always small enough such that the influence of the dispersed phase over the continuous one is negligible. Hence, the reason for introducing different representative aspects in the context of interactions with fluid particles in the following.

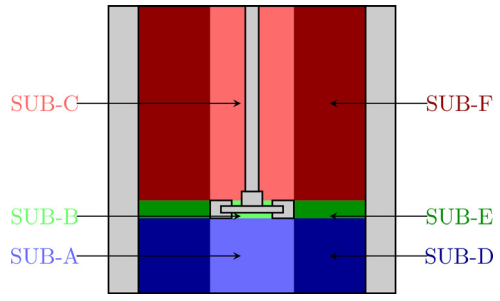

FIG. 7. Schematic representation of subdomains of potential interest as described in Table III. Subdomains A, B, C, D, E, and F colored in light blue, light green, light red, dark blue, dark green, and dark red, respectively.

A. Size and number density

Information about the size of the structures is relevant for understanding and modeling the interaction between turbulent vortices and fluid particles. For instance, in several models,[27] particle breakup is presumed to take place when the particles interact with vortices of comparable size. In this work, particular attention is paid to structures with an equivalent diameter $d_{eq} = (6V_{core}/\pi)^{1/3}$, where V_{core} is the vortex core volume, which is equal to 2, 5, and 8 mm since such structures are representative of those likely to interact with mother particles of typical size used in laboratory setups, see, e.g., Solsvik and Jakobsen[88] where the injected mother bubble diameters were in the range of 2.5–3.4 mm or Vejražka *et al.*[89] where the bubbles where in the range of 1.8–5 mm.

For different cases, Fig. 8(a) shows the resulting d_{eq} normalized by the equivalent diameter of the largest detected structure, $\max(d_{eq})$,

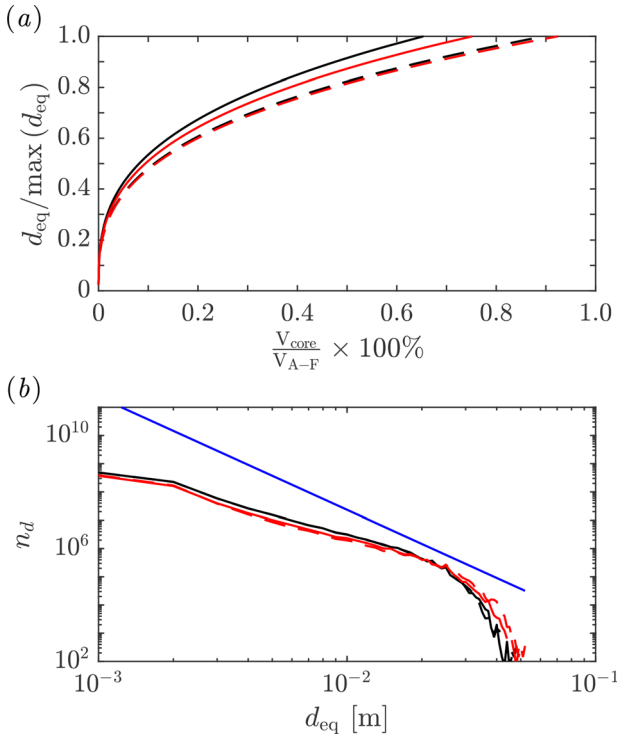

FIG. 8. Normalized size indicator and number density of the identified structures: (a) $d_{eq}/\max(d_{eq})$ vs $(V_{core}/V_{A-F}) \times 100\%$ and (b) n_d vs d_{eq}. Cases where the impeller operates at 800 and 600 rpm are identified by the line styles "——" and "- - -," respectively. Colors as explained in Table I. In (b), the blue line denotes $n_d = 24\mathcal{A}/[(2\pi)^{5/3}\mathcal{B}d_{eq}^4]$, which is the theoretical limit corresponding to the inertial subrange considering $\mathcal{A} = 1.5$[91] and $\mathcal{B} = 4.82\mathcal{A}$.[92]

as a function of the percentage volume fraction occupied by the corresponding structure, $V_{core}/V_{A-F} \times 100\%$. Here, V_{A-F} is the volume of the fluid in the subdomains A–F (see Table III). The plot includes all possible d_{eq} based on V_{core} of the structures detected in the subdomains A–F. As seen from Fig. 8(a), for a given type of fluid, an increase in N is leading to finer structures and to a decrease in the range of length scales, which is to be expected since Re is increasing as well. On the other hand, when comparing Newtonian and shear-thinning fluid cases at the same N, more sizable structures are found but not within a narrow range of length scales. This increase in size with the shear-thinning behavior is consistent with previous findings for the simpler turbulent channel flow of GN fluids (see Arosemena *et al.*[87]). Regarding the range of length scales, also for the turbulent channel flow of GN fluids, it is known that both the fluid rheology and the Reynolds number have an influence in the velocity–vorticity correlation associated with change-of-scale-effects.[90] In this case, when comparing the Newtonian and shear-thinning fluid cases at the same N, Re is probably playing a major role over the range of length scales. From a practical point of view, it is worth commenting that the size indicator, d_{eq}, appears to be in the range of $\approx$ 1 mm to 52, 47, 53, and 49 mm for cases W600, W800, C600, and C800, respectively.

Another important feature when considering the interaction with fluid particles, it is the number of structures of a given size in the stirred vessel. In the aforementioned example about particle breakup, the likelihood of the breakup event will possibly increase if the number of structures of comparable size to the mother particle is large rather than small. A quantitative indicator of the amount of vortical structures is the number density n_d defined as

$$n_d = \frac{n}{n_f V_{\text{fluid}} \Delta d_{\text{eq}}}, \tag{11}$$

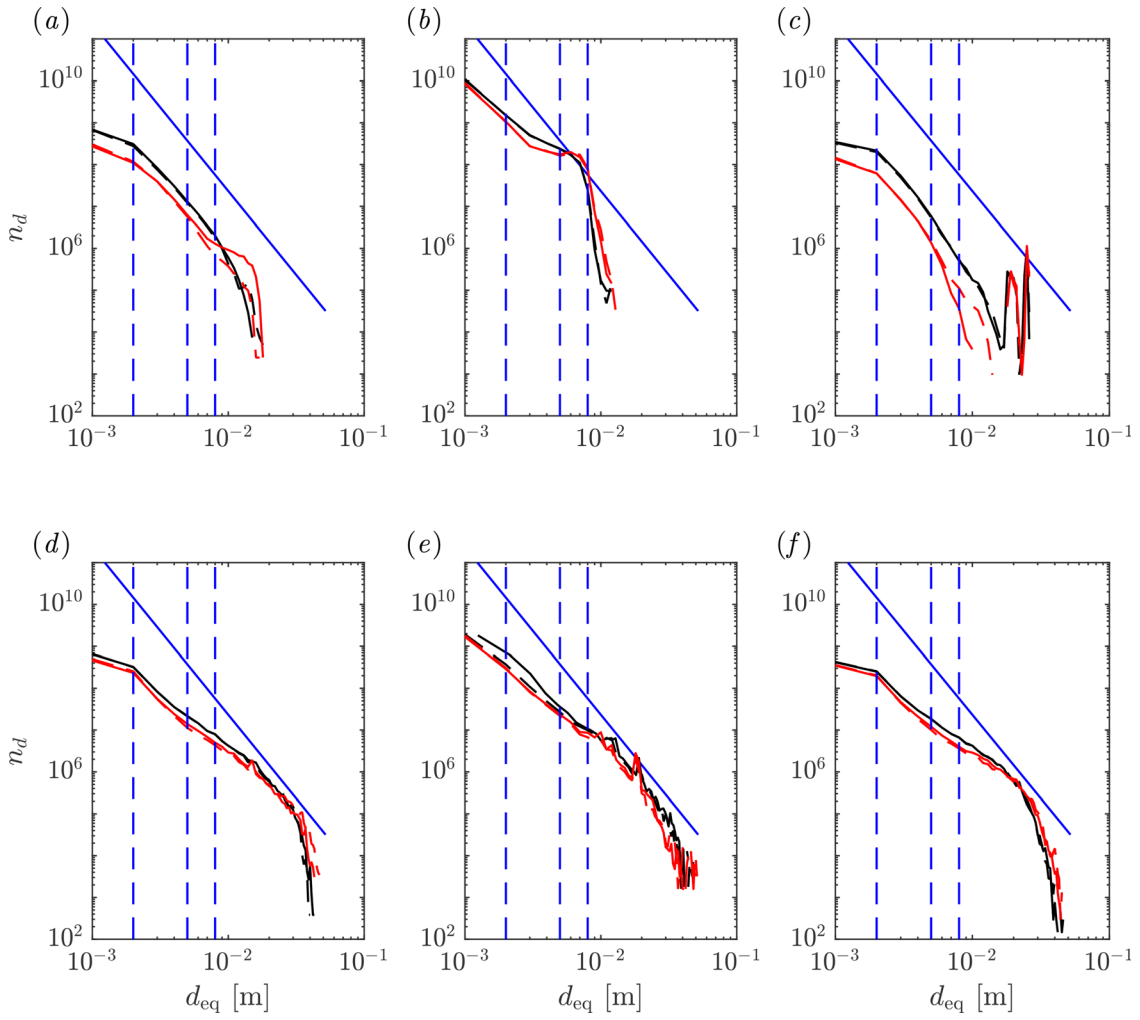

FIG. 9. Number density, n_d, as the function of the size indicator, d_{eq}, for (a) SUB-A, (b) SUB-B, (c) SUB-C, (d) SUB-D, (e) SUB-E, and (f) SUB-F. Cases where the impeller operates at 800 and 600 rpm are identified by the line styles "——" and "- - -," respectively. Colors as explained in Table I. In (a)–(f), the blue, straight line denotes $n_d = 24\mathcal{A}/[(2\pi)^{5/3}\mathcal{B}d_{eq}^4]$, which is the theoretical limit corresponding to the inertial subrange, considering $\mathcal{A} = 1.5$[91] and $\mathcal{B} = 4.82\mathcal{A}$,[92] whereas the blue, dashed lines mark values of constant d_{eq} of interest; i.e., $d_{eq} = 2, 5$, and 8 mm, respectively.

where n is the number of identified vortices of size between d_{eq} and $d_{eq} + \Delta d_{eq}$ for the collected realizations, n_f is the number of collected flow fields, V_{fluid} is the considered fluid volume within the stirred tank, i.e., $V_{fluid} = V_{A-F}$ for a number density defined in the subdomains A–F, and Δd_{eq} is the bin width for n. In other word, n_d is the time-averaged number of identified vortices of size between d_{eq} and $d_{eq} + \Delta d_{eq}$ per bin width in the considered fluid volume. Figure 8(b) displaying the number density allows us to note a monotonic decrease in n_d with increasing d_{eq} for all cases. Moreover, keeping in mind the models for n_d proposed for the whole energy spectrum,[93] we observe that the profiles appear to depict only the energy containing and inertial subranges. This is in line with the fact that large eddy simulations have been carried out. With respect to trends with fluid rheology and impeller speed, at small d_{eq} values, there is an overall decrease in the number density with shear-thinning behavior when compared to the Newtonian cases, whereas there is almost no difference in the profiles of the same fluid at different N values. Therefore, under the premise that the interaction with particles of typical size found in laboratory setups (leading to their breakup and actual mixing) is probably occurring with structures of comparable size, i.e., those having small d_{eq}, a decrease in particle breakage and dispersed–continuum phases mass transfer are expected for shear-thinning behavior in comparison with a Newtonian fluid flow operating at the same N. Recent experimental studies of bubble–liquid mass transfer[94,95] have revealed that indeed there is a decrease in bubble breakage and volumetric mass transfer coefficient with shear-thinning rheology. See trends for the bubble size distributions and the volumetric mass transfer coefficient in, e.g., Ali and Solsvik[94] for water compared to the CMC cases at the same operational conditions and axial liquid height. On the other hand, at large d_{eq}, the rapid decrease in n_d is seemingly delayed both with decreasing N and shear-thinning fluid behavior; consistently with what it is expected as the Reynolds number decreases.

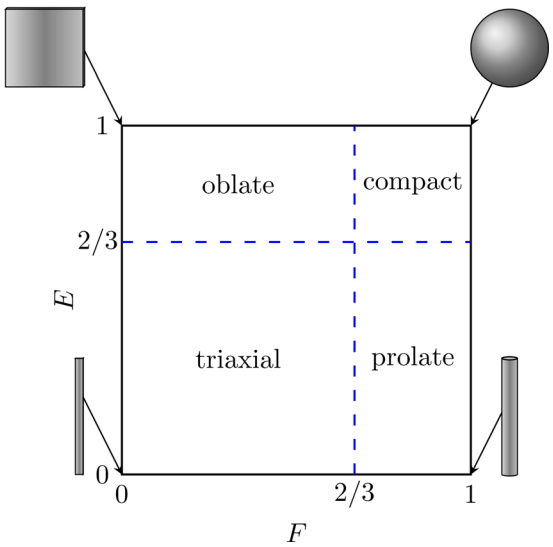

FIG. 10. Elongation, E, against flatness, F, diagram for classifying structures based on Zingg's categories.[97] The corners also illustrate the extreme cases:[78] ribbons (0,0), tubes (1,0), sheets (0,1), and spheres (1,1).

Additional insight into the interaction with fluid particles, in particular regions of the tank, can be gained by considering the n_d profile in the subdomains A–F as shown in Fig. 9. Here, aside the already noted decrease in n_d with shear-thinning behavior for $d_{eq} \lesssim 10^{-2}$ m, the following particularities are observed: (i) a wider range in d_{eq} is seen for subdomains D–F, (ii) larger n_d values for structures with $d_{eq} = 2$, 5, and 8 mm are perceived in subdomains B, D, and E, (iii) a conspicuous n_d value is noticed for $d_{eq} \approx 18$ mm in subdomain E, and (iv) for $d_{eq} \gtrsim 10^{-2}$ m, n_d appears to peak twice in subdomain C; first between 18 mm $\lesssim d_{eq} \lesssim$ 20 mm and then at $d_{eq} \approx 25$ mm. These particularities have the following (potential) implications: (i) greater range of turbulent scales for subdomains D–F, (ii) improved likelihood of particle breakage and overall mixing in subdomains B (impeller region), D and E, (iii) evidence of trailing vortices and/or remnant of them at an intermediate scale, and (iv) existence of sizable structures

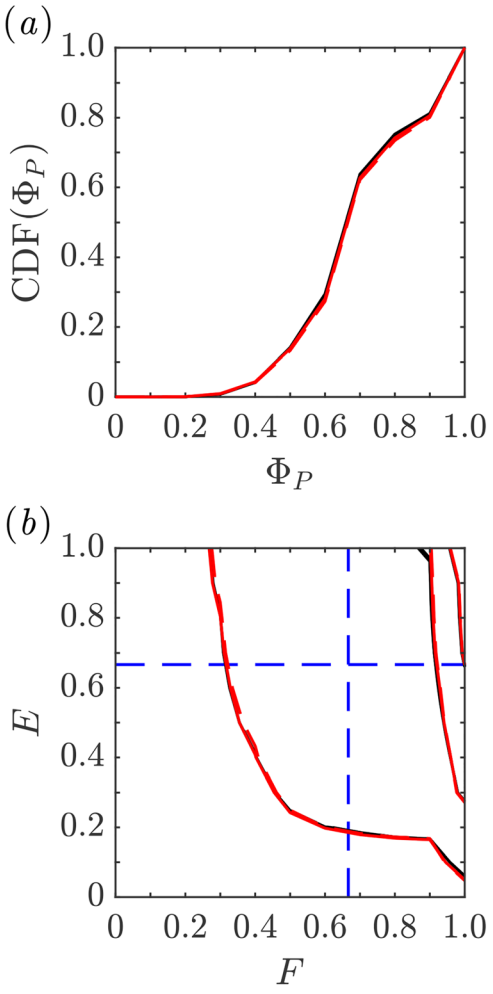

FIG. 11. Shape indicators of the identified structures across the stirred tank: (a) CDF of the maximum projection sphericity, Φ_P, and (b) JCDF of E and F, respectively. Cases where the impeller operates at 800 and 600 rpm are identified by the line styles "——" and "- - -," respectively. Colors as explained in Table I. In (b), the levels represented contain 99%, 70%, and 30% of the data. Also, the blue lines mark values of constant E and F, where E and F are equal to 2/3.

above the impeller region, probably very large structures toward the stagnation region of the tank and MI-vortex, respectively.

B. Shape

In theoretical models for breakup and coalescence of fluid particles, it is common to represent the turbulent vortices interacting with the drops or bubbles as spherical structures. Thus, the reason for using an equivalent diameter based on a spherical geometry for quantifying the size of the structures in Subsection IV A. Nonetheless, this assumption is rather questionable even for representing the largest, energy containing eddies, considering that the turbulent flow in a stirred tank is highly complex, showing different degrees of anisotropy across the vessel.[21]

Morphological analyses, typical for solid particles, include properties such as roughness, roundness (measure of the sharpness of the edges and corners of an object), and sphericity (degree to which an object approximates the shape of a sphere and measure of equidimensionality). Analogously, we can consider the sphericity and other length measurements to study the overall shape of the detected vortices. Here, the shape of the identified vortical structures is determined considering their maximum projection sphericity[96] defined as

$$\Phi_P = \left(\frac{d_S^2}{d_L d_I}\right)^{1/3}, \tag{12}$$

and their flatness and elongation parameters[97] are given by

$$F = \frac{d_S}{d_I}, \tag{13a}$$

$$E = \frac{d_I}{d_L}, \tag{13b}$$

respectively. In Eqs. (12) and (13), d_S, d_I, and d_L denote the shortest, intermediate, and largest dimensions of the oriented bounding-box (OBB) of the corresponding structure. The OBB was computed by principal component analysis (PCA), see e.g., Jolliffie.[98] The sphericity index (12) represents the ratio between the maximum projection area of a sphere of the same volume as the structure to the maximum projection area of the structure and has a maximum value of 1 for structures with the perfect spherical shape. On the other hand, the ratios F and E can be used to broadly classify the structures into four categories:[97] oblate if $F<2/3$ and $E>2/3$, compact if $F>2/3$ and $E>2/3$, triaxial if $F<2/3$ and $E<2/3$, and prolate if $F>2/3$ and $E<2/3$ (see Fig. 10). It is worth mentioning that compared to the so-called true sphericity,[99] Φ, the maximum projection sphericity is higher and lower for prolate and oblate structures, respectively. For compact and triaxial structures, $\Phi_P \approx \Phi$. Also, it is relevant to remark that in the context of turbulent structures, Moisy and Jiménez[78] proposed a similar approach to characterize the geometry of the structures. In the study, a different methodology is used to compute the lengths, d_S, d_I, and d_L, but the characterization is based on the same two dimensionless aspect ratios, F and E. In the case of ideal ribbons, tubes, sheets and spheres, these parameters are of the order of (0,0), (1,0), (0,1), and (1,1), respectively[78] (see Fig. 10).

Figure 11(a) shows the cumulative distribution function, CDF, of Φ_P across the stirred vessel for the cases described in Table I. As seen from this figure, the probability of the identified vortices being non-spherical is close to 80%, i.e., $\mathrm{CDF}(\Phi_P \leq 0.9) \approx 0.8$ for all cases. Moreover, there are two ranges in Φ_P where the probability is fairly high; one is seen for $0.6 < \Phi_P \leq 0.7$ where the probability is close to 35% and the other is seen for $0.9 < \Phi_P \leq 1.0$ corresponding to perfect spherical structures and those approaching them. With respect to the length-related parameters, Fig. 11(b) displaying the joint cumulative distribution function, JCDF, of F and E across the tank allows us to note that about 70% of the data is likely to fall into the compact and prolate categories, whereas only 30% falls into the compact category alone. The fact that $\mathrm{CDF}(\Phi_P)$ and $\mathrm{JCDF}(F, E)$ are similar for different tank rotational speeds and working fluid rheology implies that the corresponding probability density and joint probability density functions, $\mathrm{PDF}(\Phi_P)$ and $\mathrm{JPDF}(F, E)$, are also similar and, thus, suggest that the cases are statistically identical regardless of *Re* and fluid behavior. In other words, at least for the considered cases, the effects of shear-thinning rheology and Reynolds number over the shape of the identified structures in the whole tank appear negligible. In addition, Fig. 12 displaying the isocontours of $\mathrm{JPDF}(F, E)$ for case W800 allows us to observe two clear peaks; one for $0.9 < F \leq 1.0$, $0.2 < E \leq 0.3$ and another for $0.9 < F \leq 1.0$, $0.9 < E \leq 1.0$. These peaks correspond to the two aforementioned regions of high probability in Fig. 11(a). It is also worth mentioning that the expectation (mean value) for Φ_P, F, and E is 0.68, 0.83, and 0.5, respectively. To summarize, considering the information revealed by Figs. 11 and 12, although a substantial number of the detected vortices in the stirred tank present sphere-like shape, the majority do not. Furthermore, tube-like vortical structures are as likely to appear as the spherical blobs if not more so.

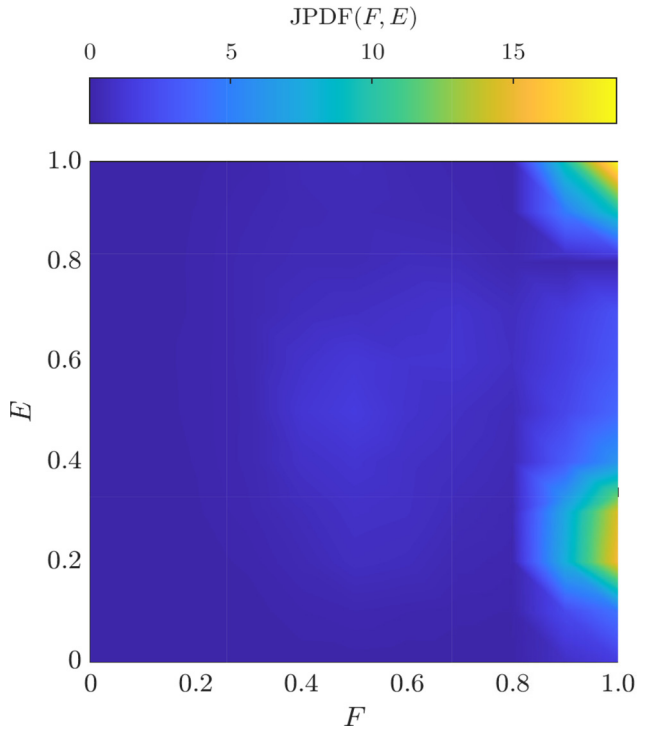

FIG. 12. Isocontours of the JPDF of E and F across the stirred tank for case W800 (see Table I).

Aside considering the form of the structures in the whole vessel, it is also reasonable to ponder which shapes are more likely to be observed locally and for those structures within a d_{eq}-range of interest. Figures 13(a)–13(f) present the JCDF(F, E) for cases W800 and C800 in different subdomains. Even though similar profiles were found when comparing Newtonian and shear-thinning cases in the entire tank, it is judged possible that these differences will arise in different subdomains and/or when considering structures of a given size in these subdomains. As seen from the figure, the probability of having compact and prolate structures remains high for all considered subdomains albeit compact structures are deemed more likely to be observed for subdomains B and E where most of the energy is contained. With respect to the influence of the shear-dependent rheology, the same figure reveals a slight increase in the likelihood of seeing more ribbon-like structures with shear-thinning rheology in the different subdomains; see consistent movement to the left and bottom of curve covering 99% of all data in subdomains A–F for case C800. Figures 13(a)–13(f) also display the peaks values of the JPDF(F, E) for a particular d_{eq}-range of interest in the subdomains A–F. In subdomain C, with independence of the fluid rheology, those structures considered to be very large and the MI-vortex appear almost and fully tubular, respectively, whereas in subdomain E, those structures hypothesized as trailing vortices seem fairly triaxial. The influence of the shear-thinning rheology over the remaining smaller structures of interest seems more complicated. On a first impression, at least to a moderate extent, it appears that structures of comparable size with $d_{eq} \lesssim 10^{-2}$ m present a different shape-related probability distribution if the fluid rheology is non-Newtonian. Nonetheless, in general, the peak of JPDF(F, E) for the considered d_{eq}-ranges in the cases W800 and C800 suggests a higher probability of the structures being more similar to ribbons and tubes than to sheets and spheres.

C. Distribution and organization in space

Under the premise that mixing is enhanced with a larger probability of interaction between vortical structures and fluid particles, a matter of practical importance is the spatial distribution of the vortices in the tank. Although it has been showed that the largest number density of vortical structures is found within subdomains B, D, and E (see Subsection IV A), information is still pending about the positioning in space where there are higher probabilities of encountering those structures. Figures 14(a)–14(f) show the marginal JCDF($r_c/D, Z_c/D$), i.e., for all possible angular positions of the centroids and where $r_c = \sqrt{X_c^2 + Y_c^2}$, in different subdomains. The figure also presents the $(r_c/D, Z_c/D)$ coordinates corresponding to peaks in the marginal JPDF($r_c/D, Z_c/D$) for a particular d_{eq}-range of interest only for cases

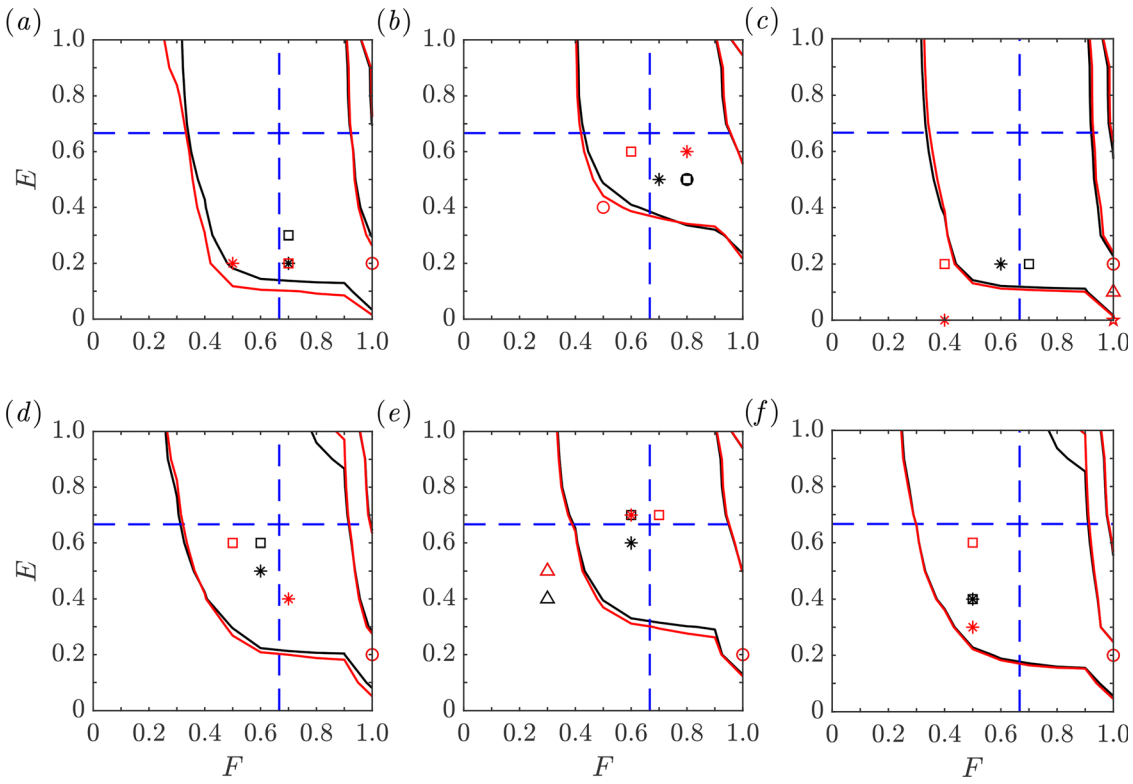

FIG. 13. JCDF of *E* and *F* for (a) SUB-A, (b) SUB-B, (c) SUB-C, (d) SUB-D, (e) SUB-E, and (f) SUB-F. The levels represented contain 99%, 70%, and 30% of the data, respectively, for cases W800 and C800. The blue lines mark values of constant *E* and *F*, where *E* and *F* are equal to 2/3. Other colors as explained in Table I. Also, the markers "∘," "∗," "□," and "⋆" are used to identify the (*E*, *F*)-values where the JPDF(F, E) peaks for d_{eq} = 2–3, 5–6, 8–9, and 25–26 mm, respectively, for cases W800 and C800. In addition and for the same cases, the "△"-marker used in (c) and (e) represents the values where the joint probability peaks for d_{eq} = 18–21 and 18–19 mm, respectively.

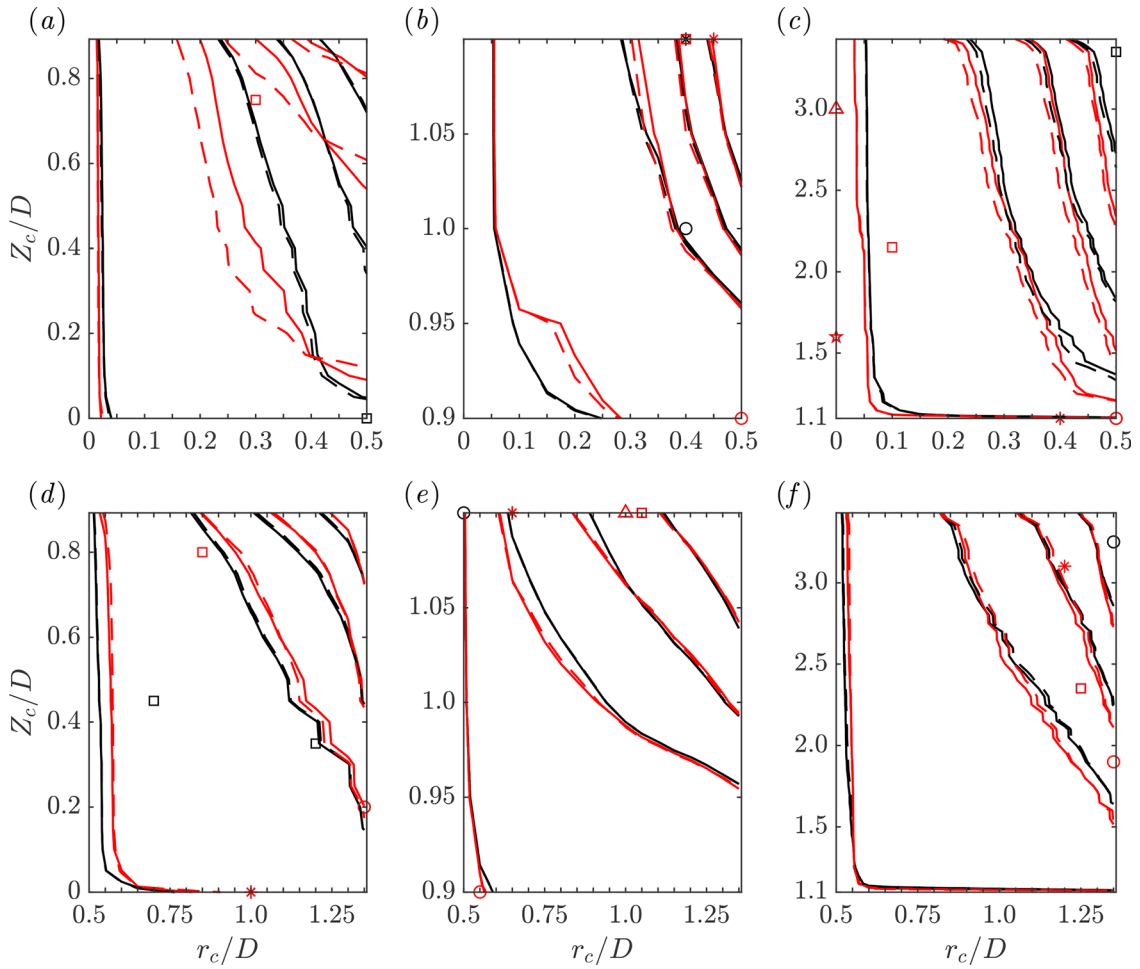

FIG. 14. Marginal JCDF of the normalized centroids in the radial and axial direction, r_c/D and Z_c/D, for (a) SUB-A, (b) SUB-B, (c) SUB-C, (d) SUB-D, (e) SUB-E, and (f) SUB-F. Cases where the impeller operates at 800 and 600 rpm are identified by the line styles "—" and "- - -," respectively. The levels represented contain 99%, 70%, 50%, and 30% of the data. Colors as explained in Table I. Also, the markers "○," "∗," "□," and "⋆" are used to identify the $(r_c/D, Z_c/D)$-values where the marginal JPDF(r_c/D, Z_c/D) peaks for d_{eq} = 2–3, 5–6, 8–9, and 25–26 mm, respectively, for cases W800 and C800. In addition and for the same cases, the "△"-marker used in (c) and (e) represents the values where the marginal joint probability peaks for d_{eq} = 18–21 and 18–19, respectively.

W800 and C800. As seen from Fig. 14, in comparison with changes in rotational speed for a given working fluid, changes in rheology for the tank operating at a specified N seem to impact the distributions in a more significant manner. Compared to the Newtonian cases for subdomains A and C, the curves covering 99% of the data move toward positions closer to the center of the tank with shear-thinning rheology, whereas the opposite behavior is observed for subdomains D and F. These trends are likely due to pronounced differences in the local flow since the changes are more evident as we approach the top and bottom walls of the stirred vessel, i.e., $Z/D \approx 3.43$ and $Z/D = 0$, respectively. On the other hand, with respect to the subdomains with the largest number density and for all cases, it is remarked that at least 70% of the data falls into $0.25 < r_c/D \leq 0.5, 0.95 < Z_c/D \leq 1.11$; $0.8 < r_c/D \leq 1.36, 0.15 < Z_c/D \leq 0.89$; and $0.6 < r_c/D \leq 1.36, 0.95 < Z_c/D \leq 1.11$ for subdomains B, D, and E, respectively. Regarding the most probable $(r_c/D, Z_c/D)$ coordinates for the considered d_{eq}-range, as with the shape indicators in Subsection IV A, a rather hectic behavior is observed. Nonetheless, for the impeller region (SUB-B), it does appear that structures with $d_{eq} \lesssim 10^{-2}$ m are likely to be detected with centroids at radial positions larger than $0.4D$. Finally, from Figs. 14(c) and 14(e) and with independence of the fluid rheology, it is remarked that structures considered to be very large and the MI-vortex appear around the center of the tank with $Z_c/D \approx 3$ and 1.6, respectively, while those structures associated with trailing vortices are probably observed with $r_c/D \approx 1$ and $Z_c/D \approx 1.1$.

Another interesting aspect, particularly when considering that high deformation and eventual breakup of fluid particles may occur due to interactions with pairing of eddies,[100] it is the organization in space of nearby structures sharing similar size. Here, the nearest structure (j) to a vortex (i) is determined by considering the minimum, absolute distance between (i), and all other detected structures (k). Thus,

$$d^{(i,j)} = \min\left(\sqrt{\left(X_c^{(k)} - X_c^{(i)}\right)^2 + \left(Y_c^{(k)} - Y_c^{(i)}\right)^2 + \left(Z_c^{(k)} - Z_c^{(i)}\right)^2}\right)$$
$$= \sqrt{\left(X_c^{(j)} - X_c^{(i)}\right)^2 + \left(Y_c^{(j)} - Y_c^{(i)}\right)^2 + \left(Z_c^{(j)} - Z_c^{(i)}\right)^2}, \quad (14)$$

where $d^{(i,j)}$ is the absolute distance between an structure (i) and the nearest one to it (j). In addition, following the works of Lozano-Durán *et al.*,[76] Dong *et al.*,[79] Osawa and Jiménez,[81] and Cheng *et al.*,[77] we consider that two structures, (i) and (j), are of similar size if their size indicator differs by less than a factor of 2, i.e., if $0.5 < d_{eq}^{(i)}/d_{eq}^{(j)} < 2$. To evaluate the likelihood of the nearest structure to vortex (i), i.e., the structure at $d^{(i,j)}$, being of similar size, we consider the PDF($\mathrm{d}_{eq}^{(i)}/\mathrm{d}_{eq}^{(j)}$) in the different subdomains and for all cases, see Figs. 15(a)–15(f). As seen from this figure, PDF($\mathrm{d}_{eq}^{(i)}/\mathrm{d}_{eq}^{(j)}$) peaks at $d_{eq}^{(i)}/d_{eq}^{(j)} \approx 1$ regardless of the case and considered subdomain in the tank. Moreover, when considering a particular subdomain, this PDF appears fairly similar for the different cases described in Table I. From Fig. 15, we also note that the probability of having the nearest structure of similar size is, at least, of 80% for SUB-A–F. As for the PDF($\mathrm{d}_{eq}^{(i)}/\mathrm{d}_{eq}^{(j)}$) corresponding to a given d_{eq}-range of interest, Fig. 15 also displays the peaks for $d_{eq} = 2$–3, $d_{eq} = 5$–6, and $d_{eq} = 8$–9 mm, respectively, for cases W800 and C800. As observed from the figure, irrespective of the subdomain and for both the cases, the probability distribution peaks within $0.5 < d_{eq}^{(i)}/d_{eq}^{(j)} < 2$ only for the lowest d_{eq}-range of interest.

Subsequently, to gain insight into the spatial organization of nearby structures sharing similar size, we will discuss their relative position with respect to the Cartesian coordinate system. The normalized relative separation between structures (i) and (j) in the X-, Y-, and Z-directions are defined as

$$dX = \frac{X_c^{(j)} - X_c^{(i)}}{d^{(i,j)}}, \quad (15a)$$

$$dY = \frac{Y_c^{(j)} - Y_c^{(i)}}{d^{(i,j)}}, \quad (15b)$$

$$dZ = \frac{Z_c^{(j)} - Z_c^{(i)}}{d^{(i,j)}}, \quad (15c)$$

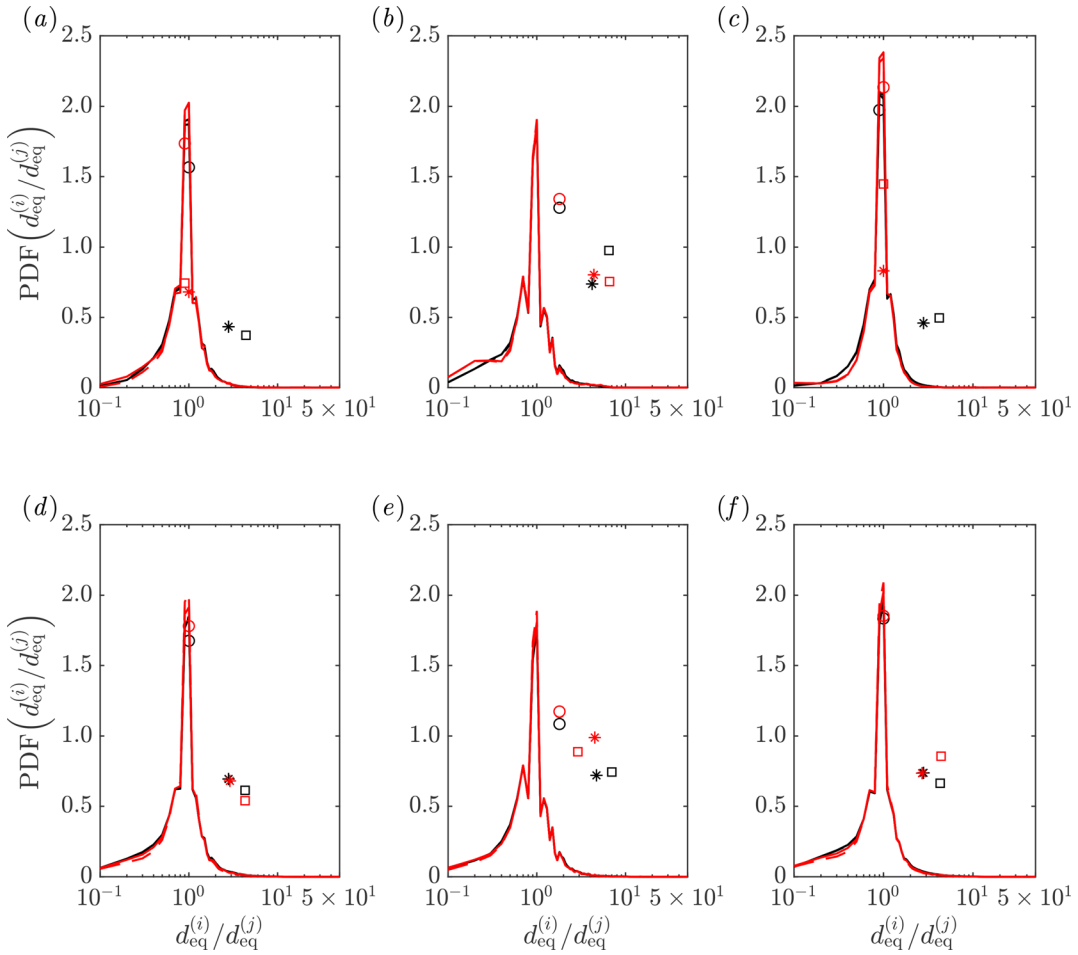

FIG. 15. PDF of ratio between the size indicator of a vortex "i" to the nearest vortex "j" to it, $d_{eq}^{(i)}/d_{eq}^{(j)}$, for (a) SUB-A, (b) SUB-B, (c) SUB-C, (d) SUB-D, (e) SUB-E, and (f) SUB-F. Cases where the impeller operates at 800 and 600 rpm are identified by the line styles "——" and "- - -," respectively. Colors as explained in Table I. Also, the markers "○," "∗," and "□" are used to identify the $d_{eq}^{(i)}/d_{eq}^{(j)}$-values where the PDF($\mathrm{d}_{eq}^{(i)}/\mathrm{d}_{eq}^{(j)}$) peaks for $d_{eq} = 2$–3, 5–6, and 8–9 mm in cases W800 and C800.

respectively. From the perspective of analytic geometry, relationships (15) represent the direction cosines of a straight line joining the centroids of structures (i) and (j). As a consequence, these relationships range from –1 to 1 for corresponding direction angles ranging from π to 0. For SUB-A–F, Fig. 16 shows the marginal probabilities, PDF(dX), PDF(dY), and PDF(dZ). We remark that the figure only displays the marginal probabilities for case W800 since similar distributions were found for cases W600, C600, and C800 (not shown here). As seen from the figure, for all subdomains, PDF(dX) and PDF(dY) seem statistically identical and the largest values in these marginal probabilities are observed for dX and dY equal to $-\sqrt{2}/2, 0$, and $\sqrt{2}/2$. In contrast and with respect to PDF(dZ), the marginal probability always peaks at $dZ = 0$ and, only for subdomains B and E, peaks at $dZ = \pm\sqrt{2}/2$ are moderately discernible. We emphasize that these finding about the marginal probabilities only indicate which direction cosine is more probable when considering all possible values for the two remaining direction cosines. Nonetheless, the consistent peaks at dX and dY equal to $\pm\sqrt{2}/2$ and the fact that, in the Z-direction, the most likely outcome appears to be a right angle with the nearest structures of similar size, it is already conveying. Figure 17 shows the marginal JPDF(dX, dZ) for case W800 and the subdomains with the largest number density, SUB-B, -D, and -E. As displayed by this figure, the global maxima of the marginal joint distributions for these subdomains are the same and occur at $dX \approx \pm\sqrt{2}/2, dZ = 0$. Likewise, for subdomain E, additional local maxima is clearly observed at $dX = 0, dZ \approx \pm\sqrt{2}/2$. Recalling that only two of the three direction cosines are independent, it is expected that $dY = \pm dX$ for the global maxima and $dY = \pm dZ$ for the additional maxima in SUB-E. These findings imply a high probability of encountering the nearest structures having similar size, side-by-side in the radial direction. Furthermore, these pairs of nearest structures having similar size are unlikely to overlap and seem organized both in the X and Y directions with separation of about $d^{(i,j)}$. It is worth mentioning that based on the other found maxima, at least for SUB-E, it is probable to encounter nearest structures having similar size on top of each other without perfect alignment of their centroids. Also, considering the similarities between the marginal distributions for subdomains A, C, D, and

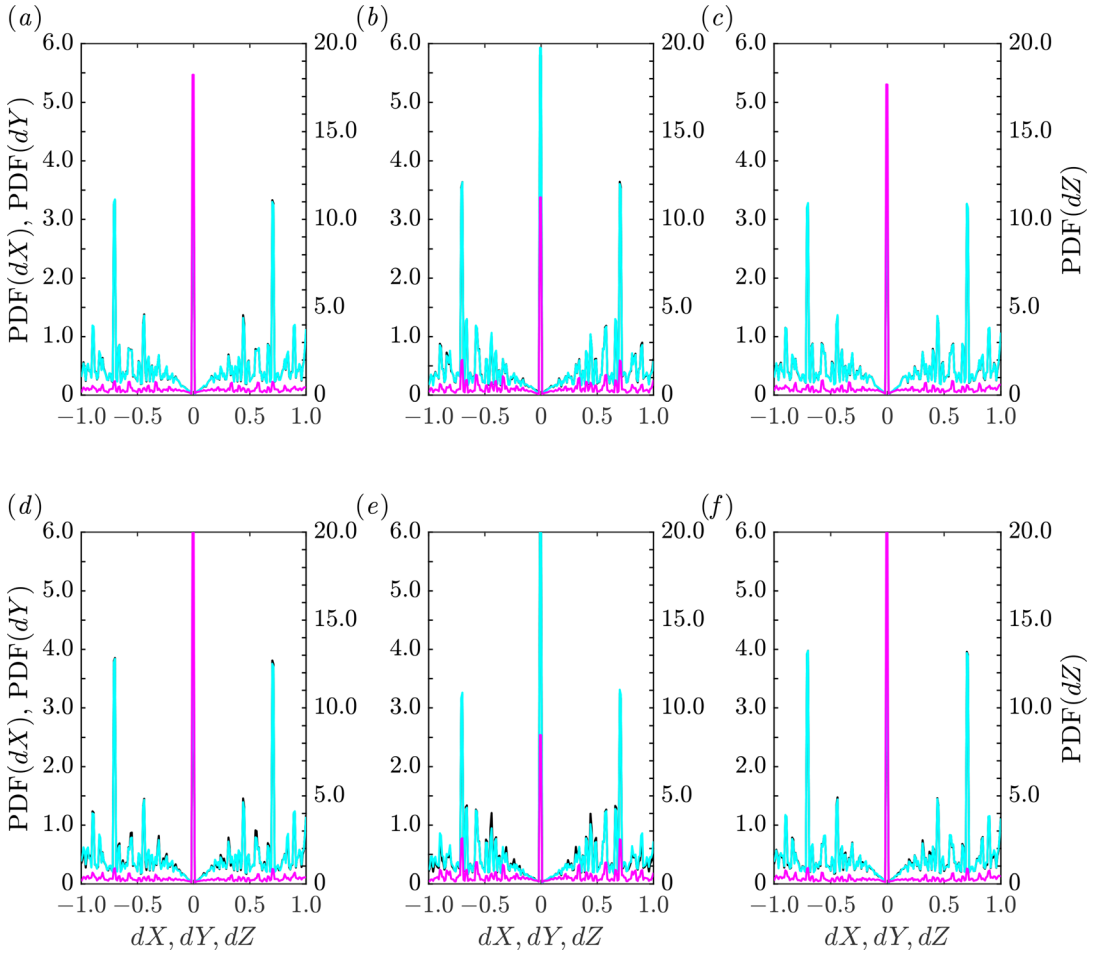

FIG. 16. Marginal PDF of the normalized relative separation between nearest structures of similar size, dX, dY, and dZ, for case W800 as described in Table I and for (a) SUB-A, (b) SUB-B, (c) SUB-C, (d) SUB-D, (e) SUB-E, and (f) SUB-F. Black, cyan, and magenta colors are used to represent the profiles corresponding to the marginal probabilities of dX, dY, and dZ, respectively.

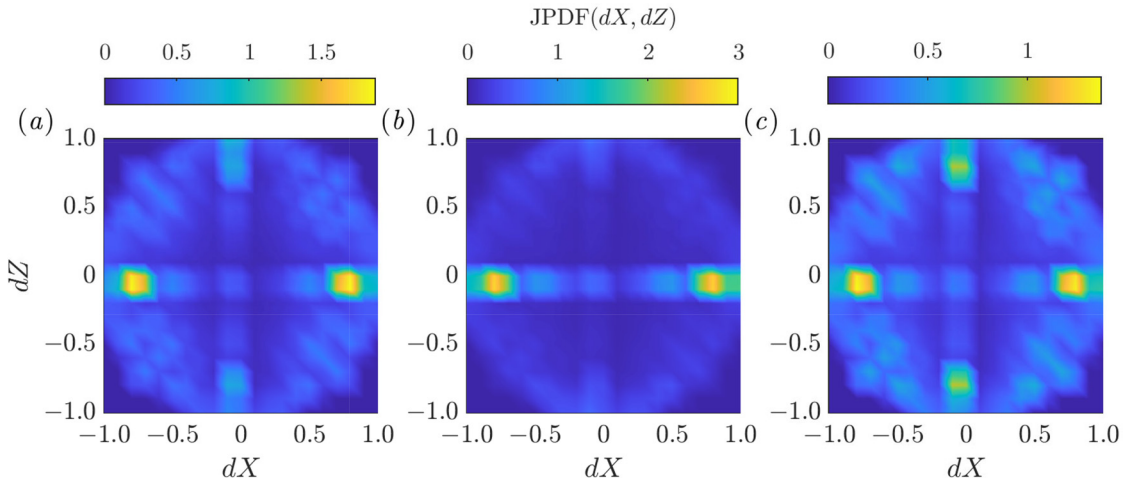

FIG. 17. Isocontours of the marginal JPDF of *dX* and *dZ* for case W800 as described in Table I and for (a) SUB-B, (b) SUB-D, and (c) SUB-E.

F (see Fig. 16), a similar organization as the one observed for SUB-D is expected for SUB-A, -C, and -F.

D. Correlation with kinetic energy

Finally, when thinking about dispersion of fluid particles and actual mixing in a stirred vessel, it is important to explore whether the identified structures are positioned in regions with high energy contents or not. Many criteria for deformation and eventual breakup of drops and bubbles are based on energy balances between the fluid particles and the surrounding eddies, see e.g., Liao and Lucas[25] and Solsvik *et al.*[27] In this work, to address the degree of correlation between the identified vortices and the kinetic energy due to turbulence and the periodic blade passage (associated with the trailing vortices), we consider the following correlation coefficient:

$$\mathcal{C}_{\mathrm{Q}_\star k} = \frac{\mathrm{cov}(\mathrm{Q}_\star, k)}{\mathrm{stv}(\mathrm{Q}_\star)\mathrm{stv}(k)}, \tag{16}$$

where $\mathrm{cov}(\mathrm{Q}_\star, k)$ is the covariance or mixed second moment of $\mathrm{Q}_\star$ subject to condition (10) and $k = (u_i - \exp(u_i))^2/2$, i.e., the instantaneous kinetic energy due to turbulent fluctuations and the periodic component imposed by the frequency of the blade passages. Here, $\mathrm{stv}(k)$ is the standard deviation of k and $\exp(u_i)$ is the expectation or time-averaged value for u_i. The correlation coefficient is a statistical indicator about the degree of (linear) correlation between two stochastic variables. If the coefficient is zero, the variables are entirely irrelevant (in a linear sense), whereas if it is 1, they are perfectly correlated. In the case where the coefficient is -1, the variables are perfectly negatively correlated and the increase in one leads to the (linear) decrease in the other. As a consequence, $\mathcal{C}_{\mathrm{Q}_\star k}$ is a practical tool to determine how closely related is the vortex indicator, $\mathrm{Q}_\star$, to k.

For the regions exhibiting the largest number density of structures, the circumferential averages $\langle\,\rangle_\theta$, i.e., averages over the angular direction θ, corresponding to $\mathcal{C}_{\mathrm{Q}_\star k}$ and k are presented in Figs. 18–20 for cases W600, W800, and C800. In these figures, $\langle k\rangle_\theta$ is normalized by its local maximum, $\max_{SUB}\langle k\rangle_\theta$, in that particular subdomain. As displayed by the figures, the isocontours corresponding to cases W600 and W800 seem quite similar, whereas case C800 presents some differences. For the shear-thinning case, more discernible patches of moderate correlation values are observed at larger radial distances and the regions of high kinetic energy seem more localized. Nonetheless, regardless of the case and for $r/D \gtrsim 0.25$, positive and fairly high correlation values are noted in the subdomain occupied by the impeller. Moreover, such a region, where the passage of the blades takes place, appears as the most energetic in SUB-B, see Figs. 18(d)–20(d). With respect to subdomains D and E, the largest correlation values are also seen in the vicinity of the most energetic regions for the three cases, see Figs. 18(b)–20(b), 18(c)–20(c), 18(e)–20(e), and 18(f)–20(f). In addition, also for subdomains D and E, it is observed that low correlation regions corresponds to those with low energy contents but a high distribution of vortical structures (see Subsection IV C). Overall, these findings suggest that strong vortices in the sense of how much their rotation rate exceeds their strain rate are detected in regions with a significant amount of k, and in such regions, a linear approximation between $\mathrm{Q}_\star$ and k may be reasonable to some extent. Conversely, as one moves from the impeller region and k solely represents turbulent kinetic energy, its correlation with the vortex indicator is rather poor. Of course, this does not imply that $\mathrm{Q}_\star$ and k are independent but just that the relationship between them is nonlinear, which is in chord with our understanding of the direct cascade process.

V. FINAL REMARKS

Instantaneous flow fields have been considered to identify and characterize vortical structures. The flow fields, collected after quasi-steady state conditions are achieved, correspond to large eddy simulations of a laboratory-scale, baffled, stirred tank with a Rushton-type impeller. In simulations, the tank operates under turbulent flow conditions (at least in the region near the impeller) either at 600 or 800 rpm and with water or 0.2 wt. % CMC solution as the working fluid. Thus, changes in the detected structures arising due to variations of the tank rotational speed and the fluid rheology are explored as well.

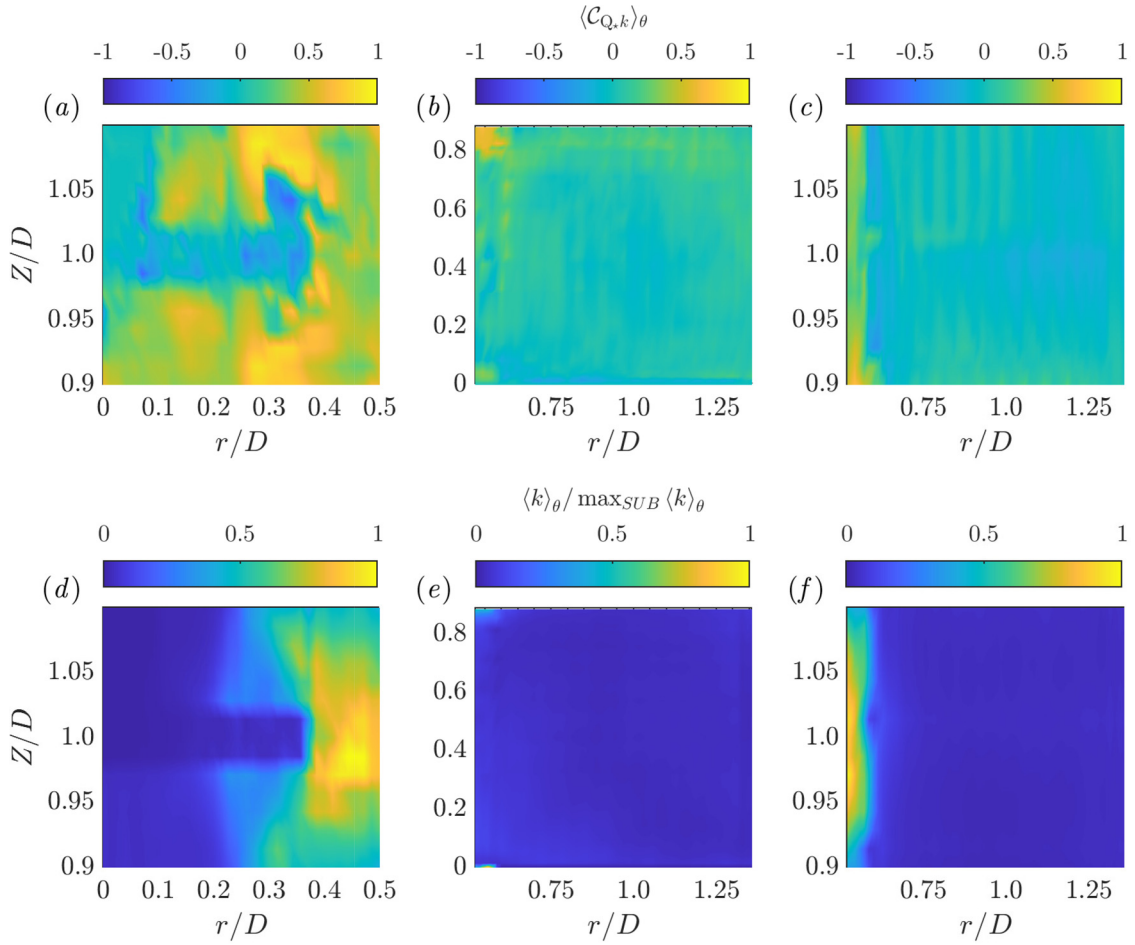

FIG. 18. Isocontours of the circumferential average, $\langle\,\rangle_\theta$, corresponding to the correlation coefficient between the considered vortex criterion, $Q_\star$, and the kinetic energy due to turbulence and the periodic passage of the blades, k, and normalized k: (a)–(c) $\langle \mathcal{C}_{Q_\star k} \rangle_\theta$ and (d)–(f) $\langle k \rangle_\theta / \max_{SUB} \langle k \rangle_\theta$. (a) and (d), (b) and (e), and (c) and (f) correspond to SUB-B, -D, and -E, respectively. Case W600 as described in Table I. In (a), for visualization purposes, 3D undefined positions; i.e., those in regions occupied by the shaft and disk of the impeller, have been set to 0 before taking the circumferential average.

The identification of the structures is performed using an objectivized version of the traditional Q-criterion,[58] which also takes into account that the flow in a stirred tank is inhomogeneous in all spatial directions. The implemented method is believed to yield consistent results even if slightly different threshold values are used. The characterization of the detected structures, involving aspects such as size, number density, shape, spatial organization, and correlation with kinetic energy, is done through different statistical analyses. Our main findings can be summarized as follows:

(i) Considering a size indicator based on the equivalent diameter of a sphere, the largest detected structures seem to be about the same order of magnitude as the impeller diameter, whereas the smallest identified structures appear to be about one order of magnitude less than D. Moreover, finer structures within a narrower range of length scales are observed with an increase of the impeller rotational speed for the same working fluid. Regarding the effect of shear-thinning rheology respect to a Newtonian case operating at the same N, more sizable structures are detected but not within a narrower range of length scales. This latter observation is explained in terms of the Reynolds number playing a more important role than the fluid rheology when compared to Newtonian and shear-thinning cases operating at the same N.

(ii) The profiles obtained for the number density as a function of the size indicator, covering different subdomains under study in the stirred tank, appear to depict only the energy containing and inertial subranges. This observation is in line with the fact that LES are performed. For the smallest detected scales, the effect of changing N for the same working fluid seems negligible while a change from Newtonian to shear-thinning rheology for the tank operating at the same N leads to an overall decrease in n_d. On the other

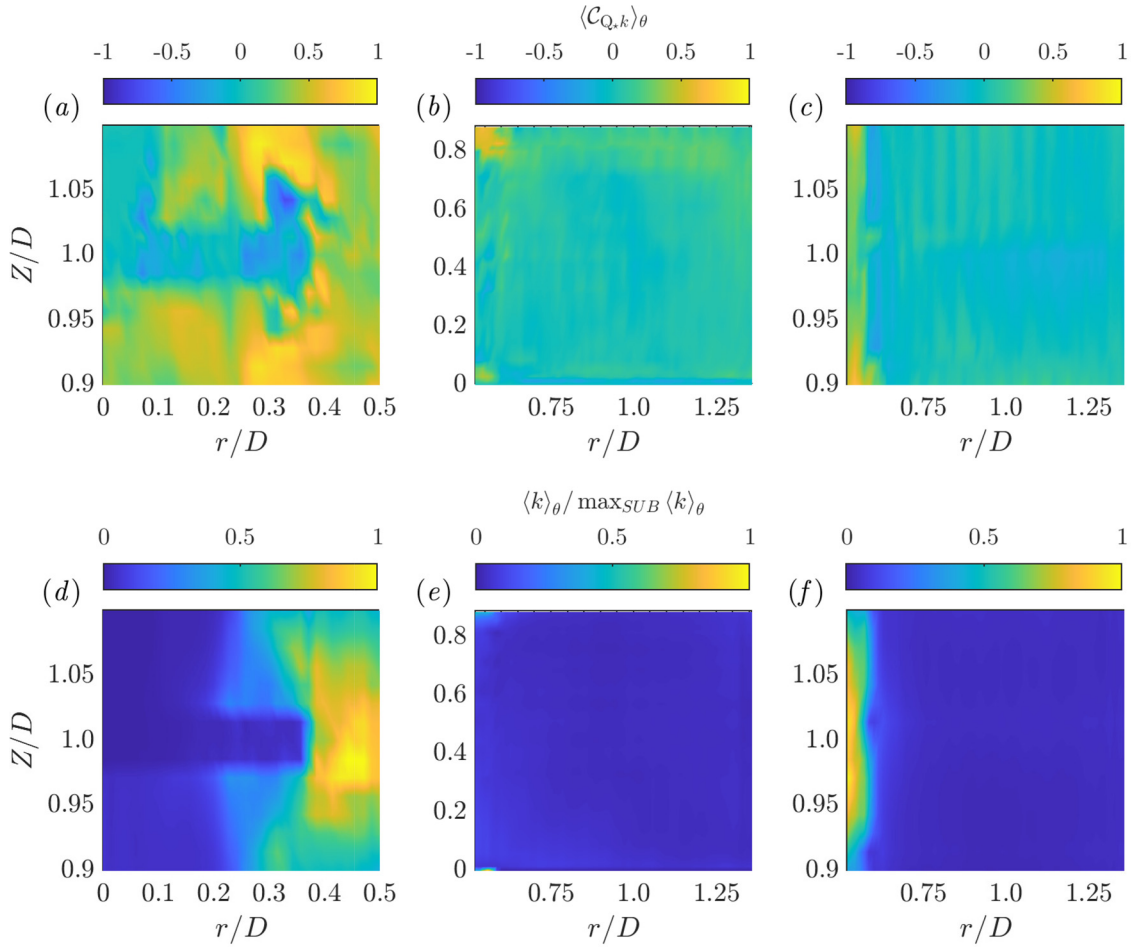

FIG. 19. Isocontours of the circumferential average, $\langle\,\rangle_\theta$, corresponding to the correlation coefficient between the considered vortex criterion, $Q_\star$, and the kinetic energy due to turbulence and the periodic passage of blades, k, and normalized k: (a)–(c) $\langle \mathcal{C}_{Q_\star k} \rangle_\theta$ and (d)–(f) $\langle k \rangle_\theta / \max_{SUB} \langle k \rangle_\theta$. (a) and (d), (b) and (e), and (c) and (f) correspond to SUB-B, -D, and -E, respectively. Case W800 as described in Table I. In (a), for visualization purposes, 3D undefined positions, i.e., those in regions occupied by the shaft and disk of the impeller, have been set to 0 before taking the circumferential average.

hand, at large values of d_{eq}, the rapid decrease in n_d is seemingly delayed both with decreasing N and shear-thinning fluid behavior. This observation is consistent with what we expect as the Reynolds number decreases.

(iii) Also, with respect to n_d but for particular regions of the tank, the largest values in n_d are observed in subdomains B, D, and E (see Table III) for structures having d_{eq} of about one order of magnitude less than D. n_d profile is also given for a wider range of d_{eq} in subdomains D–F, and conspicuous values of n_d are achieved in subdomains C and E, which are hypothesized to be related to MI and trailing vortices, respectively (see Fig. 9).

(iv) In regard to the shape of the detected structures based on the flatness and elongation parameters (see Subsection IV B), tube-like vortical structures are as likely to appear as spherical blobs if not more so. Furthermore, when considering particular subdomains in the tank, only for subdomains B and E—where most of the energy is contained—it is found that sphere-like structures are more likely to be observed. It is also worth remarking that the structures considered MI and trailing vortices appear fully tubular and fairly triaxial, respectively [see Figs. 13(c) and 13(e)]. On the other hand, the effect of shear-thinning rheology as compared to a Newtonian case operating at the same N seems to lead to more ribbon-like structures in different subdomains of the tank.

(v) Respecting the spatial distribution of structures within subdomains having largest n_d, it is remarked that at least 70% of the data covering all angular positions fall into $0.25 < r_c/D \leq 0.5, 0.95 < Z_c/D \leq 1.11$; $0.8 < r_c/D \leq 1.36$, $0.15 < Z_c/D \leq 0.89$; and $0.6 < r_c/D \leq 1.36, 0.95 < Z_c/D \leq 1.11$ for subdomains B, D, and E, respectively. Moreover, in comparison with changes in rotational speed for a given working fluid, changes in rheology for the tank operating at

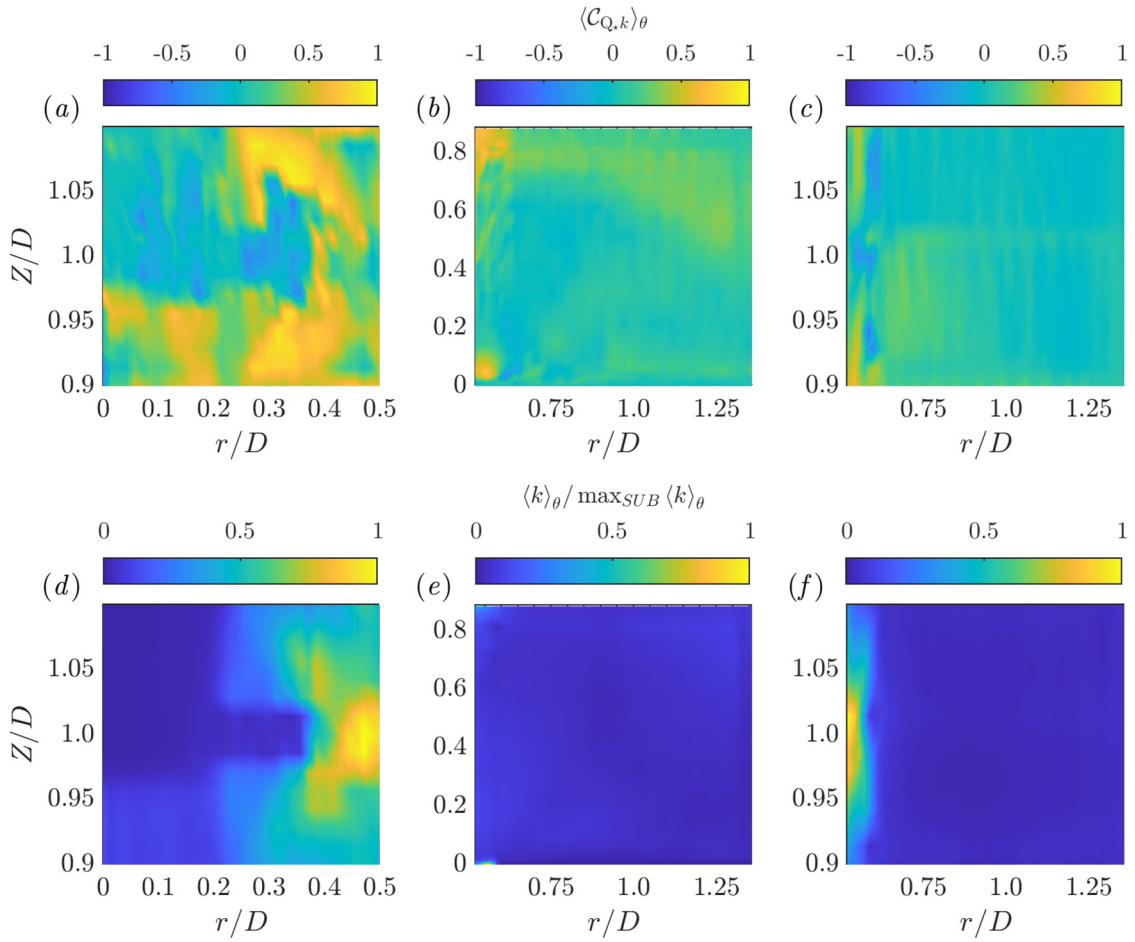

FIG. 20. Isocontours of the circumferential average, $\langle\,\rangle_\theta$, corresponding to the correlation coefficient between the considered vortex criterion, Q_*, and the kinetic energy due to turbulence and the periodic passage of blades, k, and normalized k: (a)–(c) $\langle \mathcal{C}_{Q_*k} \rangle_\theta$ and (d)–(f) $\langle k \rangle_\theta / \max_{SUB} \langle k \rangle_\theta$. (a) and (d), (b) and (e), and (c) and (f) correspond to SUB-B, -D, and -E, respectively. Case C800 as described in Table I. In (a), for visualization purposes, 3D undefined positions, i.e., those in regions occupied by the shaft and disk of the impeller, have been set to 0 before taking the circumferential average.

a specified N appear to impact the distributions in a more significant manner (see Subsection IV C).

(vi) In term of spatial organization, it is found that the nearest structure to another detected one shares the same size and are likely to be side-by-side in the radial direction. Furthermore, these pairs of nearest structures having similar size are unlikely to overlap and seem organized both in the X and Y directions with a separation of about the minimum absolute distance between a pair [see Eq. (14)]. Additionally, it is worth commenting that for subdomain E, the probability of encountering nearest structures having similar size on top of each other but without perfect alignment of their centroids is high as well.

(vii) With respect to the correlation between the vortex indicator and the kinetic energy due to turbulence and the periodic component, positive and fairly high correlation values are observed in regions with high energy contents for subdomains B, D, and E, i.e., the subdomains having largest n_d. These results suggest that, at least to some extent and for regions with the local high energy content, a linear relationship between the vortex indicator and this kinetic energy may be reasonable.

Although the above findings correspond to simulations of the single-phase, turbulent flow of the Newtonian and shear-thinning fluids in a baffled stirred tank reactor, the potential implications for liquid–liquid and gas–liquid dispersed systems are worth pondering. This is particularly the case when considering one-way coupling in which the influence of the dispersed phase over the continuous one is negligible, i.e., for multiphase systems where the local fraction of the dispersed phase (holdup) is always sufficiently small. Hence, in the case of one-way coupling, some of the aforementioned findings possibly imply the following:

(i) There is a higher probability of fluid particle breakage in subdomains B, D, and E where the number density is the largest for the smallest detected structures, i.e., those having

a size indicator of about one order of magnitude less than D. This statement, of course, is only valid under the premise that the interaction with particles of typical size found in laboratory setups (leading to their deformation and eventual breakup) is indeed occurring with structures of comparable size.

(ii) It is questionable to assume that vortical structures interacting with fluid particles present spherical shape. Perhaps such assumption, common in some phenomenological models used to predict fluid particle breakage rate and size distributions (consider, e.g., Luo and Svendsen[101]) should be limited to regions of high energy content in the stirred vessel such as subdomains B and E. Moreover, breakage models where turbulent vortices would be described as tube-like structures instead of spherical ones are also worth exploring when considering the energy containing scales and when moving beyond them. A reasonable starting point would be to consider non-spherical vortex models for isotropic turbulence, see, e.g., Saffman.[102]

(iii) The probability of pairs of vortices sharing similar size and interacting with fluid particles seems fairly high. Moreover, the spatial organization of these pairing is such that the odds of encountering several pairs in the vicinity of a fluid particle is also high. These are aspects that should be accounted for in models for breakup of bubbles and droplets in turbulent flows.

(iv) Optimal feeding points for fluids particles would be those where the probability of detecting the structures—of a similar size to the particles under consideration—is fairly large but more so where the correlation between the vortex indicator and the energy content is high as well. Such tentative feeding points can be found by cross-referencing the results presented Subsections IV C and IV D.

Finally, we would like to highlight some natural extensions of the present work. On one side, since the input flow fields are obtained from LES and not DNS, the smallest structures at the dissipative scales are yet to be analyzed. In addition, in light of recent studies about reconstruction of 3D flow fields in stirred vessels using proper orthogonal decomposition (POD),[103–105] it would be interesting to explore the identification and characterization of vortical structures based on reconstructed DNS flow fields corresponding to different POD modes (not just the first and most energetic ones). Conversely, the previous implications are just potential outcomes and require corroboration by means of experimentation and/or proper simulations of turbulent dispersions in stirred tank reactors. Moreover, even though recent DNS of single inertial drops in isotropic turbulence have shown that local patches of swirling fluid provide the main source for particle deformation, see plausible reinterpretation of the arrival/bombarding eddies of Luo and Svendsen[101] as "outer" eddies by Vela-Martín and Avila,[106] vortices or swirling-like structures are not necessarily the only type of flow structure that plays an active role in the deformation and breakup of fluid particles.

ACKNOWLEDGMENTS

This work was supported by the Research Council of Norway (RCN, Grant No. 274398). The authors are grateful for computer resources provided by Sigma2 (Grant No. NN9771K) and by local cluster, Idun,[107] at NTNU. The authors would like to thank Professor C. Liu and his group at the University of Texas at Arlington for providing the FORTRAN code, "Objective-OmegaUTA". Although the code was not used, it allowed better understanding the procedure to objectivize any Eulerian vortex identification method.

AUTHOR DECLARATIONS

Conflict of Interest

The authors have no conflicts to disclose.

DATA AVAILABILITY

The data that support the findings of this study are available from the corresponding author upon reasonable request.

NOMENCLATURE

Abbreviations

CDF	Cumulative distribution function
CMC	Carboxymethyl cellulose
cov	Covariance
DNS	Direct numerical simulations
exp	Expectation/mean
GN	Generalized Newtonian
JCDF	Joint cumulative distribution function
JPDF	Joint probability density function
LES	Large-eddy simulations
MI/MIs	Macroinstability/macroinstabilities
MRF	Multiple reference frame
PDF	Probability density function
RANS	Reynolds-averaged Navier–Stokes simulations
SGS	Subgrid-scales
SM	Sliding mesh
stv	Standard deviation
SUB	Subdomain

Greek letters

$\dot{\gamma} = (2S_{ij}S_{ij})^{1/2}$	Strain rate $(1/s)$
μ_a	Fluid apparent dynamic viscosity (Pa s), see Eq. (6)
ρ	Fluid density (kg/m^3)
Φ_P	Maximum projection sphericity, see Eq. (12)

Other symbols

C	Off-bottom clearance (cm)
$\mathcal{C}_{Q_\star k}$	Correlation coefficient between $Q_\star$ and k, see Eq. (16)
C600,C800	CMC flow cases under study, see Table I
D	Impeller diameter (cm)
D_i	Impeller diameter (cm) without blades
D_{ij}	Velocity gradient tensor $(1/s)$
$d_{eq} = (6V_{core}/\pi)^{1/3}$	Equivalent diameter (m) of a vortical structures.

$d_{eq}^{(i)}, d_{eq}^{(j)}$	d_{eq} of a vortex (i) and d_{eq} of the nearest vortex to it (j)
$d^{(i,j)}$	Absolute distance (m) between a vortex (i) and the nearest one to it (j), see Eq. (14)
DS_i	Shaft inner diameter (cm)
dX, dY, dZ	Normalized relative separation between a vortex (i) and the nearest one to it (j), see Eq. (15)
F, E	Flatness and elongation parameters, see Eq. (13)
h_b	Blades height (cm)
k	In Subsection IV D, kinetic energy (m/s) due to turbulence and the periodic blade passage
N	Impeller rotational speed (rev/s)
n_d	Number density per number of temporal realizations (per m^4 s) of vortical structures
$Q_\star$	Objective version of Q-criterion of Hunt *et al.*[58] (1/s), see Eq. (9). Also, vortex indicator when inequality (10) is fulfilled
$r = \sqrt{X^2 + Y^2}$	Radial coordinate (m)
$r_c = \sqrt{X_c^2 + Y_c^2}$	Radial coordinate (m) of the centroid of a vortical structure
Re	Reynolds number, see Table I
S_{ij}	Strain rate tensor (1/s), symmetric part of D_{ij}
T	Stirred tank diameter (cm)
$\mathcal{T}$	Threshold parameter, see inequality (10)
t_b	Blades thickness (cm)
u_i	Instantaneous velocity field (m/s). After Subsection II D, $u_i \equiv \widetilde{u}_i$
V_{A-F}	Volume of fluid (m^3) within subdomains A–F, see Table III
V_{core}	Vortex core volume (m^3)
w_b	Blades width (cm)
W600,W800	Water flow cases under study, see Table I
X, Y, Z	Cartesian coordinates (m), see Fig. 1
X_c, Y_c, Z_c	Centroid (m) of a vortical structure in Cartesian coordinates
$\theta = \tan^{-1}(Y/X)$	Angular coordinate (rad)
$\widetilde{\ }$	Grid filtering operator in the context of LES

REFERENCES

[1] R. P. Chhabra and J. F. Richardson, "Liquid mixing," in *Non-Newtonian Flow and Applied Rheology* (Butterworth-Heinemann, 2008), pp. 376–461.
[2] J. M. Nouri and J. H. Whitelaw, "Particle velocity characteristics of dilute to moderately dense suspension flows in stirred reactors," Int. J. Multiphase Flow **18**, 21–33 (1992).
[3] M. Soos, R. Kaufmann, R. Winteler, M. Kroupa, and B. Lüthi, "Determination of maximum turbulent energy dissipation rate generated by a Rushton impeller through large eddy simulation," AIChE J. **59**, 3642–3658 (2013).
[4] D. Fernandes del Pozo, A. Liné, K. M. Van Geem, C. L. Men, and I. Nopens, "Hydrodynamic analysis of an axial impeller in a non-Newtonian fluid through particle image velocimetry," AIChE J. **66**, e16939 (2020).
[5] S. Hara, S. Ebihara, and Y. Kawaguchi, "Influence of viscoelasticity on mixing performance of primary and secondary circulation flows in stirred vessels," Phys. Fluids **32**, 075102 (2020).
[6] M. Schäfer, M. Höfken, and F. Durst, "Detailed LDV measurements for visualization of the flow field within a stirred-tank reactor equipped with a Rushton turbine," Chem. Eng. Res. Des. **75**, 729–736 (1997).
[7] K. V. Sharp and R. J. Adrian, "PIV study of small-scale flow structure around a Rushton turbine," AIChE J. **47**, 766–778 (2001).
[8] B. C. H. Venneker, J. J. Derksen, and H. E. A. Van den Akker, "Turbulent flow of shear-thinning liquids in stirred tanks—The effects of Reynolds number and flow index," Chem. Eng. Res. Des. **88**, 827–843 (2010).
[9] A. de Lamotte, A. Delafosse, S. Calvo, and D. Toye, "Analysis of PIV measurements using modal decomposition techniques, POD and DMD, to study flow structures and their dynamics within a stirred-tank reactor," Chem. Eng. Sci. **178**, 348–366 (2018).
[10] P. Mavros, "Flow visualization in stirred vessels: A review of experimental techniques," Chem. Eng. Res. Des. **79**, 113–127 (2001).
[11] F. Sbrizzai, V. Lavezzo, R. Verzicco, M. Campolo, and A. Soldati, "Direct numerical simulation of turbulent particle dispersion in an unbaffled stirred-tank reactor," Chem. Eng. Sci. **61**, 2843–2851 (2006).
[12] J. J. J. Derksen and H. E. A. Van den Akker, "Direct numerical simulation of the turbulent flow in a baffled tank driven by a Rushton turbine," AIChE J. **58**, 3878–3890 (2012).
[13] A. Tamburini, G. Gagliano, G. Micale, A. Brucato, F. Scargiali, and M. Ciofalo, "Direct numerical simulations of creeping to early turbulent flow in unbaffled and baffled stirred tanks," Chem. Eng. Sci. **192**, 161–175 (2018).
[14] J. G. M. Eggels, "Direct and large-eddy simulation of turbulent fluid flow using the lattice-Boltzmann scheme," Int. J. Heat Fluid Flow **17**, 303–323 (1996).
[15] J. Derksen and H. E. A. Van den Akker, "Large eddy simulations on the flow driven by a Rushton turbine," AIChE J. **45**, 209–221 (1999).
[16] H. Hartmann, J. J. Derksen, C. Montavon, J. Pearson, I. S. Hamill, and H. E. A. van den Akker, "Assessment of large eddy and rans stirred tank simulations by means of LDA," Chem. Eng. Sci. **59**, 2419–2432 (2004).
[17] R. Sungkorn, J. J. Derksen, and J. G. Khinast, "Modeling of aerated stirred tanks with shear-thinning power law liquids," Int. J. Heat Fluid **36**, 153–166 (2012).
[18] H. Singh, D. F. Fletcher, and J. J. Nijdam, "An assessment of different turbulence models for predicting flow in a baffled tank stirred with a Rushton turbine," Chem. Eng. Sci. **66**, 5976–5988 (2011).
[19] A. Tamburini, A. Brucato, M. Ciofalo, G. Gagliano, G. Micale, and F. Scargiali, "CFD simulations of early- to fully-turbulent conditions in unbaffled and baffled vessels stirred by a Rushton turbine," Chem. Eng. Res. Des. **171**, 36–47 (2021).
[20] F. Garcia-Ochoa and E. Gomez, "Bioreactor scale-up and oxygen transfer rate in microbial processes: An overview," Biotechnol. Adv. **27**, 153–176 (2009).
[21] R. Escudié and A. Liné, "Analysis of turbulence anisotropy in a mixing tank," Chem. Eng. Sci. **61**, 2771–2779 (2006).
[22] J.-C. Gabelle, J. Morchain, D. Anne-Archard, F. Augier, and A. Liné, "Experimental determination of the shear rate in a stirred tank with a non-Newtonian fluid: Carbopol," AIChE J. **59**, 2251–2266 (2013).
[23] I. Takashima and M. Mochizuki, "Tomographic observations of the flow around agitator impeller," J. Chem. Eng. Jpn. **4**, 66–72 (1971).
[24] L. F. Richardson, "The fundamental equations: The effects of eddy motion," in *Weather Prediction by Numerical Process* (Cambridge University Press, 1922), p. 66.
[25] Y. Liao and D. Lucas, "A literature review of theoretical models for drop and bubble breakup in turbulent dispersions," Chem. Eng. Sci. **64**, 3389–3406 (2009).
[26] Y. Liao and D. Lucas, "A literature review on mechanisms and models for the coalescence process of fluid particles," Chem. Eng. Sci. **65**, 2851–2864 (2010).
[27] J. Solsvik, S. Tangen, and H. A. Jakobsen, "On the constitutive equations for fluid particle breakage," Rev. Chem. Eng. **29**, 241–356 (2013).
[28] S. M. Kresta and R. S. Brodkey, "Turbulence in mixing applications," in *Handbook of Industrial Mixing: Science and Practice*, edited by E. L. Paul, V. A. Atiemo-Obeng, and S. M. Kresta (John Wiley & Sons, 2004), pp. 44–45.
[29] K. Van't Riet and J. M. Smith, "The behaviour of gas–liquid mixtures near Rushton turbine blades," Chem. Eng. Sci. **28**, 1031–1037 (1973).
[30] K. Van't Riet and J. M. Smith, "The trailing vortex system produced by Rushton turbine agitator," Chem. Eng. Sci. **30**, 1093–1105 (1975).

[31]K. Van't Riet, W. Bruijn, and J. M. Smith, "Real and pseudo-turbulence in the discharge stream from a Rushton turbine," Chem. Eng. Sci. **31**, 407–412 (1976).
[32]M. Yianneskis, Z. Popiolek, and J. H. Whitelaw, "An experimental study of the steady and unsteady flow characteristics of stirred reactors," J. Fluid Mech. **175**, 537–555 (1987).
[33]C. M. Stoots and R. V. Calabrese, "Mean velocity field relative to a Rushton turbine blade," AIChE J. **41**, 1–11 (1995).
[34]K. C. Lee and M. Yianneskis, "Turbulence properties of the impeller stream of a Rushton turbine," AIChE J. **44**, 13–24 (1998).
[35]J. J. Derksen, M. S. Doelman, and H. E. A. Van den Akker, "Three-dimensional LDA measurements in the impeller region of a turbulently stirred tank," Exp. Fluids **27**, 522–532 (1999).
[36]R. Escudié and A. Liné, "Experimental analysis of hydrodynamics in a radially agitated tank," AIChE J. **49**, 585–603 (2003).
[37]R. Escudié, D. Bouyer, and A. Liné, "Characterization of trailing vortices generated by a Rushton turbine," AIChE J. **50**, 75–85 (2004).
[38]Y. Bouremel, M. Yianneskis, and A. Ducci, "On the utilisation of vorticity and strain dynamics for improved analysis of stirred processes," Chem. Eng. Res. Des. **87**, 377–385 (2009).
[39]K. V. Sharp, D. Hill, D. Troolin, G. Walters, and W. Lai, "Volumetric three-component velocimetry measurements of the turbulent flow around a Rushton turbine," Exp. Fluids **48**, 167–183 (2010).
[40]Z. Chara, B. Kysela, J. Konfrst, and I. Fort, "Study of fluid flow in baffled vessels stirred by a Rushton standard impeller," Appl. Math. Comput. **272**, 614–628 (2016).
[41]L. Nikiforaki, G. Montante, K. C. Lee, and M. Yianneskis, "On the origin, frequency and magnitude of macro-instabilities of the flows in stirred vessels," Chem. Eng. Sci. **58**, 2937–2949 (2003).
[42]C. Galletti, A. Paglianti, K. C. Lee, and M. Yianneskis, "Reynolds number and impeller diameter effects on instabilities in stirred vessels," AIChE J. **50**, 2050–2063 (2004).
[43]A. Ducci and M. Yianneskis, "Vortex tracking and mixing enhancement in stirred processes," AIChE J. **53**, 305–315 (2007).
[44]Z. Doulgerakis, M. Yianneskis, and A. Ducci, "On the interaction of trailing and macro-instability vortices in a stirred vessel-enhanced energy levels and improved mixing potential," Chem. Eng. Res. Des. **87**, 412–420 (2009).
[45]F. Irgens, "Generalized Newtonian fluids," In *Rheology and non-Newtonian Fluids* (Springer, 2014), pp. 113–125.
[46]J. Smagorinsky, "General circulation experiments with the primitive equations. I: The basic experiment," Mon. Weather Rev. **91**, 99–165 (1963).
[47]D. K. Lilly, "On the application of the eddy viscosity concept in the inertial subrange of turbulence," Technical Report No. NCAR MS 123 (National Centre for Atmospheric Research, Boulder, CO, 1966).
[48]J. Fan, Y. Wang, and W. Fei, "Large eddy simulations of flow instabilities in a stirred tank generate by a Rushton turbine," Chin. J. Chem. Eng. **15**, 200–208 (2007).
[49]T. T. Devi and B. Kumar, "Large-eddy simulation of turbulent flow in stirred tank with a curved blade impeller," J. Eng. Thermophys. **24**, 152–168 (2015).
[50]A. B. Metzner and R. E. Otto, "Agitation of non-Newtonian fluids," AIChE J. **3**, 3–10 (1957).
[51]C. Yang and Z.-S. Mao, "Multiphase stirred reactors," in *Numerical Simulation of Multiphase Reactors with Continuous Liquid Phase* (Academic Press, 2014), pp. 75–151.
[52]J. Y. Luo, R. I. Issa, and A. D. Gosman, "Prediction of impeller induced flows in mixing vessels using multiple frames of reference," in *Proceedings of 8th European Conference on Mixing* (InTech, 1994), pp. 549–556.
[53]J. Y. Murthy, S. R. Mathur, and D. Choudhury, "CFD simulation of flows in stirred tank reactors using a sliding mesh technique," in *Proceedings of 8th European Conference on Mixing* (InTech, 1994), pp. 341–348.
[54]M. Moštěk, A. Kukuková, M. Jahoda, and V. Machoň, "Comparison of different techniques for modelling of flow field and homogenization in stirred vessels," Chem. Pap. **59**, 380–385 (2005), see https://www.chempap.org/?id=7&paper=13.
[55]B. E. Launder and D. B. Spalding, "The numerical computation of turbulent flows," Comput. Methods Appl. Mech. Eng. **3**, 269–289 (1974).
[56]V. Holmén, "Methods for vortex identification," Master's thesis (Lund University, 2012).
[57]B. P. Epps, "Review of vortex identification methods," in 55th AIAA Aerospace Sciences Meeting, 2017.
[58]J. C. R. Hunt, A. A. Wray, and P. Moin, "Eddies, streams and convergence zones in turbulent flows," in *Center for Turbulence Research, Proceedings of the Summer Program* (NASA Ames Research Center, 1988), pp. 193–208.
[59]M. S. Chong, A. E. Perry, and B. J. Cantwell, "A general classification of three–dimensional flow fields," Phys. Fluids A **2**(5), 765–777 (1990).
[60]J. Jeong and F. Hussain, "On the identification of a vortex," J. Fluid Mech. **285**, 69–94 (1995).
[61]J. Zhou, R. J. Adrian, S. Balachandar, and T. M. Kendall, "Mechanisms for generating coherent packets of hairpin vortices in channel flow," J. Fluid Mech. **387**, 353–396 (1999).
[62]P. Chakraborty, S. Balachandar, and R. J. Adrian, "On the relationships between local vortex identification schemes," J. Fluid Mech. **535**, 189–214 (2005).
[63]V. Kolář, "Vortex identification: New requirements and limitations," Int. J. Heat Fluid Flow **28**, 638–652 (2007).
[64]G. Haller, "An objective definition of a vortex," J. Fluid Mech. **525**, 1–26 (2005).
[65]C. Liu, Y. Wang, Y. Yang, and Z. Duan, "New omega vortex identification method," Sci. China–Phys. Mech. Astron. **59**, 684711 (2016).
[66]T. Günther, M. Schulze, and H. Theisel, "Rotation invariant vortices for flow visualization," IEEE Trans. Visual Comput. Graphics **22**, 817–826 (2016).
[67]G. Haller, "Can vortex criteria be objectivized?," J. Fluid Mech. **908**, A25 (2021).
[68]G. Haller, A. Hadjighasem, M. Farazmand, and F. Huhn, "Defining coherent vortices objectively from the vorticity," J. Fluid Mech. **795**, 136–173 (2016).
[69]J. Liu, Y. Gao, and C. Liu, "An objective version of the vortex vector for vortex identification," Phys. Fluids **31**, 065112 (2019).
[70]J. Liu, Y. Gao, Y. Wang, and C. Liu, "Objective omega vortex identification method," J. Hydrodyn. **31**, 455–463 (2019).
[71]C. Liu, Y. Gao, S. Tian, and X. Dong, "Rortex—A new vortex vector definition and vorticity tensor and vector decompositions," Phys. Fluids **30**, 035103 (2018).
[72]S. Tian, Y. Gao, X. Dong, and C. Liu, "Definitions of vortex vector and vortex," J. Fluid Mech. **849**, 312–103 (2018).
[73]Y. Gao and C. Liu, "Rortex and comparison with eigenvalue based vortex identification criteria," Phys. Fluids **30**, 085107 (2018).
[74]R. Nagaosa and R. A. Handler, "Statistical analysis of coherent vortices near a free surface in a fully developed turbulence," Phys. Fluids **15**, 375–394 (2003).
[75]J. C. del Álamo, J. Jiménez, P. Zandonade, and R. D. Moser, "Self-similar vortex clusters in the turbulent logarithmic region," J. Fluid Mech. **561**, 329–358 (2006).
[76]A. Lozano-Durán, O. Flores, and J. Jiménez, "The three-dimensional structure of momentum transfer in turbulent channels," J. Fluid Mech. **694**, 100–130 (2012).
[77]C. Cheng, W. Li, A. Lozano-Durán, and H. Liu, "On the structure of streamwise wall-shear stress fluctuations in turbulent channel flows," J. Fluid Mech. **903**, A29 (2020).
[78]F. Moisy and J. Jiménez, "Geometry and clustering of intense structures in isotropic turbulence," J. Fluid Mech. **513**, 111–133 (2004).
[79]S. Dong, A. Lozano-Durán, A. Sekimoto, and J. Jiménez, "Coherent structures in statistically stationary homogeneous shear turbulence," J. Fluid Mech. **816**, 167–208 (2017).
[80]J. Hwang and H. J. Sung, "Wall-attached structures of velocity fluctuations in a turbulent boundary layer," J. Fluid Mech. **856**, 958–983 (2018).
[81]K. Osawa and J. Jiménez, "Intense structures of different momentum fluxes in turbulent channels," Phys. Rev. Fluids **3**, 084603 (2018).
[82]R. Escudié and A. Liné, "A simplified procedure to identify trailing vortices generated by a Rushton turbine," AIChE J. **53**, 523–526 (2007).
[83]S. Başbuğ, G. Papadakis, and J. C. Vassilicos, "DNS investigation of the dynamical behaviour of trailing vortices in unbaffled stirred vessels at transitional Reynolds numbers," Phys. Fluids **29**, 064101 (2017).
[84]A. Zamiri and J. T. Chung, "Numerical evaluation of turbulent flow structures in a stirred tank with a Rushton turbine based on scale-adaptive simulation," Comput. Fluids **170**, 236–248 (2018).

[85]T. Mihalić, Z. Guzović, and A. Predin, "Performances and flow analysis in the centrifugal vortex pump," J. Fluids Eng. **135**, 011107 (2013).
[86]L. Wang, C. Guo, Y. Su, and T. Wu, "A numerical study on the correlation between the evolution of propeller trailing vortex wake and skew of propellers," Int. J. Nav. Archit. Ocean Eng. **10**, 212–214 (2018).
[87]A. A. Arosemena, R. Andersson, H. I. Andersson, and J. Solsvik, "Effects of shear-thinning rheology on near-wall turbulent structures," J. Fluid Mech. **925**, A37 (2021).
[88]J. Solsvik and H. A. Jakobsen, "Single air bubble breakup experiments in stirred water tank," Int. J. Chem. React. **13**, 477–491 (2015).
[89]J. Vejražka, M. Zedníková, and P. Stanovský, "Experiments on breakup of bubbles in a turbulent flow," AIChE J. **64**, 740–757 (2018).
[90]A. A. Arosemena and J. Solsvik, "Velocity–vorticity correlations and the four-layer regime in turbulent channel flow of generalized Newtonian fluids," Eur. J. Mech. B **91**, 1–8 (2022).
[91]H. Tennekes and J. L. Lumley, *A First Course in Turbulence* (MIT Press, 1972).
[92]G. K. Batchelor, *The Theory of Homogeneous Turbulence* (CUP, 1982).
[93]J. Solsvik and H. A. Jakobsen, "A review of the statistical turbulence theory required extending the population balance closure models to the entire spectrum of turbulence," AIChE J. **62**, 1795–1820 (2016).
[94]H. Ali and J. Solsvik, "Axial distributions of bubble–liquid mass transfer coefficient in laboratory-scale stirred tank with viscous Newtonian and non-Newtonian fluids," Phys. Fluids **32**, 123308 (2020).
[95]H. Ali and J. Solsvik, "Bubble hydrodynamics and mass transfer in stirred tank with non-Newtonian fluids: Scale-up from laboratory to pilot-scale," Phys. Fluids **33**, 033319 (2021).
[96]E. D. Sneed and R. L. Folk. Pebbles in the lower Colorado river, Texas: A study in particle morphogenesis. J. Geol. **66**, 114–150 (1958).
[97]T. Zingg, "Beitrag zur schotteranalyse," PhD thesis (ETH, Zurich, 1935).
[98]I. T. Jolliffe, *Principal Component Analysis* (Springer, 2002).
[99]H. Wadell, "Volume, shape, and roundness of rock particles," J. Geol. **40**, 443–451 (1932).
[100]R. Andersson and B. Andersson, "Modeling the breakup of fluid particles in turbulent flows," AIChE J. **52**, 2031–2038 (2006).
[101]H. Luo and H. F. Svendsen, "Theoretical model for drop and bubble breakup in turbulent dispersions," AIChE J. **42**, 1225–1233 (1996).
[102]P. G. Saffman, "Vortex models of isotropic turbulence," Philos. Trans. R. Soc., London A **355**, 1949–1956 (1997).
[103]G. Janiga, "Large-eddy simulation and 3D proper orthogonal decomposition of the hydrodynamics in a stirred tank," Chem. Eng. Sci. **201**, 132–144 (2019).
[104]K. Mikhaylov, S. Rigopoulos, and G. Papadakis, "Reconstruction of large-scale flow structures in a stirred tank from limited sensor data," AIChE J. **67**, e17348 (2021).
[105]C. Mayorga, J. Morchain, and A. Liné, "Reconstruction of the 3D hydrodynamics in a baffled stirred tank using proper orthogonal decomposition," Chem. Eng. Sci. **248**, 117220 (2022).
[106]A. Vela-Martín and M. Avila, "Deformation of drops by outer eddies in turbulence," J. Fluid Mech. **929**, A38 (2021).
[107]M. Själander, M. Jahre, G. Tufte, and N. Reissmann, "EPIC: An energy-efficient, high-performance GPGPU computing research infrastructure," arXiv:1912.05848.